MCB
Journals.ASM.org

Quantitative *In Vivo* Fluorescence Cross-Correlation Analyses Highlight the Importance of Competitive Effects in the Regulation of Protein-Protein Interactions

Wakako Sadaie,[a] Yoshie Harada,[b] Michiyuki Matsuda,[a,b,c] Kazuhiro Aoki[d]

Laboratory of Bioimaging and Cell Signaling, Graduate School of Biostudies, Kyoto University, Sakyo-ku, Kyoto, Japan[a]; Institute for Integrated Cell-Material Sciences (WPI-iCeMS), Kyoto University, Sakyo-ku, Kyoto, Japan[b]; Department of Pathology and Biology of Diseases, Graduate School of Medicine, Kyoto University, Sakyo-ku, Kyoto, Japan[c]; Imaging Platform for Spatio-Temporal Information, Graduate School of Medicine, Kyoto University, Sakyo-ku, Kyoto, Japan[d]

Computer-assisted simulation is a promising approach for clarifying complicated signaling networks. However, this approach is currently limited by a deficiency of kinetic parameters determined in living cells. To overcome this problem, we applied fluorescence cross-correlation spectrometry (FCCS) to measure dissociation constant (K_d) values of signaling molecule complexes in living cells (*in vivo* K_d). Among the pairs of fluorescent molecules tested, that of monomerized enhanced green fluorescent protein (mEGFP) and HaloTag-tetramethylrhodamine was most suitable for the measurement of *in vivo* K_d by FCCS. Using this pair, we determined 22 *in vivo* K_d values of signaling molecule complexes comprising the epidermal growth factor receptor (EGFR)–Ras–extracellular signal-regulated kinase (ERK) mitogen-activated protein (MAP) kinase pathway. With these parameters, we developed a kinetic simulation model of the EGFR-Ras-ERK MAP kinase pathway and uncovered a potential role played by stoichiometry in Shc binding to EGFR during the peak activations of Ras, MEK, and ERK. Intriguingly, most of the *in vivo* K_d values determined in this study were higher than the *in vitro* K_d values reported previously, suggesting the significance of competitive bindings inside cells. These *in vivo* K_d values will provide a sound basis for the quantitative understanding of signal transduction.

The epidermal growth factor (EGF) receptor (EGFR)–Ras–extracellular signal-regulated kinase (ERK) mitogen-activated protein (MAP) kinase pathway plays pleiotropic roles in cell functions such as cell proliferation, differentiation, survival, and tumorigenesis (1–3). This signaling pathway has been extensively studied, and vast amounts of proteins and regulations have been identified, resulting in an increase in the pathway's complexity. Computer-assisted simulation is one of the most promising approaches for the comprehensive understanding of the signal transduction pathway as a system. Indeed, a number of simulation models of the EGFR-Ras-ERK MAP kinase pathway have been reported over the past 10 years (4–7). In these simulation models, most of the kinetic parameters used for numerical simulations were not measured experimentally but rather were assumed by fitting the experimental data with the simulation data or simply determined arbitrarily. Consequently, there are substantial differences in the parameters among these studies, making it difficult to evaluate these simulation models quantitatively.

The kinetic parameters used for the simulation of intracellular signal transduction include protein concentrations, enzymatic kinetics, diffusion coefficients, and dissociation constants of the protein-protein interactions, which are denoted K_d. Among them, K_d is of central importance, because protein-protein interactions are a major constituent of signal transduction pathways (8). Under steady-state conditions, the K_d of the simple binding between protein A and protein B is defined as

$$\mathrm{A} + \mathrm{B} \underset{k_b}{\overset{k_f}{\rightleftharpoons}} \mathrm{AB} \tag{1}$$

$$K_d = \frac{[\text{Free A}][\text{Free B}]}{[\text{AB}]} \tag{2}$$

$$K_d = \frac{k_b}{k_f} \tag{3}$$

where k_f and k_b are association and dissociation rate constants, respectively, and [Free A], [Free B], and [AB] correspond to the concentrations of unbound free protein A, protein B, and protein AB complexes, respectively. According to these definitions, the smaller the K_d values, the higher the affinity of the protein-protein interaction.

The K_d value has been determined by *in vitro* experiments such as coprecipitation experiments, sedimentation equilibrium using analytical ultracentrifugation, surface plasmon resonance (SPR), and isothermal titration calorimetry (ITC). All of these *in vitro* methods enable us to acquire the K_d value (here referred to as the "*in vitro* K_d" value) (Fig. 1A). The *in vitro* K_d value reflects the strength of the protein-protein interaction determined by the intrinsic properties of the two proteins. On the other hand, a few reports have measured dissociation constants in living cells (here referred to as the "*in vivo* K_d") (Fig. 1B) by means of intermolecular fluorescence resonance energy transfer (FRET), single-molecule fluorescence imaging, and fluorescence cross-correlation spectroscopy (FCCS) (9–12). All of these techniques employ two-color fluorescence imaging. Theoretically, the *in vivo* K_d can be affected mainly by two factors: competitive binding and molecular

Received 16 January 2014 Returned for modification 25 February 2014
Accepted 16 June 2014
Published ahead of print 23 June 2014
Address correspondence to Kazuhiro Aoki, k-aoki@lif.kyoto-u.ac.jp.

doi:10.1128/MCB.00087-14

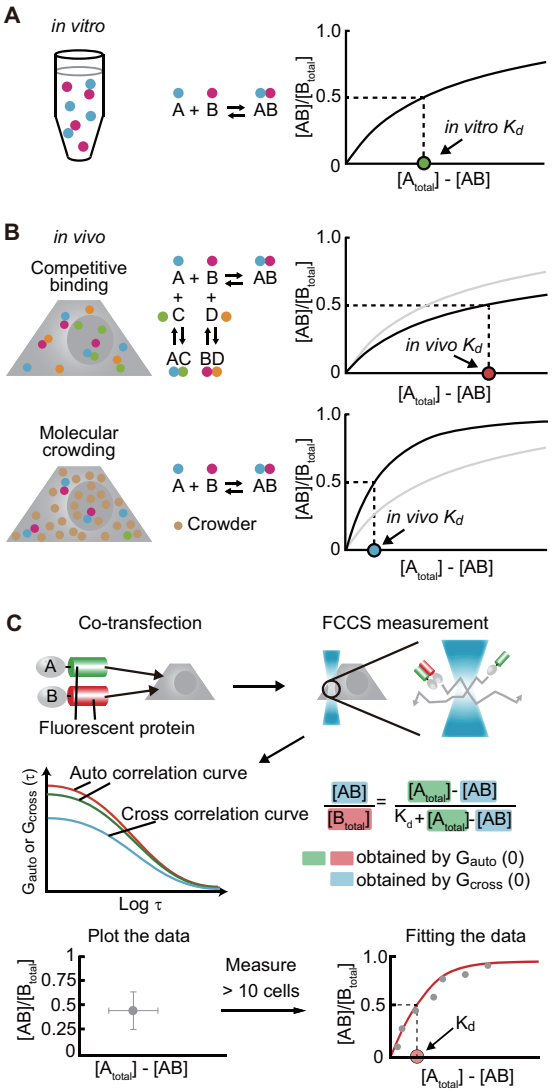

FIG 1 Strategy for measuring *in vivo* K_d by FCCS. (A and B) Comparison between *in vitro* K_d (A) and *in vivo* K_d (B) values. In general, the *in vivo* K_d was affected by competitive binding proteins (B, top) and molecular crowding (B, bottom), leading to increased and decreased of K_d values compared to the *in vitro* K_d values (A), respectively. (C) Experimental procedure for measurement of *in vivo* K_d by FCCS. HeLa cells were cotransfected with two plasmids expressing fluorescent protein-fused proteins A and B. Two days after transfection, the cells were subjected to FCCS measurements. At least 5 points in the cytoplasm of each cell were analyzed by FCCS. In each cell, the concentrations of total A protein ($[A_{total}]$), total B protein ($[B_{total}]$), and the protein AB complex ([AB]) were obtained by the *y* intercepts of the autocorrelation curves (red and green curves) and cross-correlation curve (blue curve), respectively. The averaged values of the ratios of [AB] to $[B_{total}]$ in each cell, with standard deviations, are plotted against the unbound A protein concentration ($[A_{total}] - [AB]$), with standard deviations. The K_d value was obtained by fitting the data to equations 16 and 17.

crowding (Fig. 1B). In the former case, non-fluorescently labeled proteins, including endogenous and other interacting proteins, bind competitively to fluorescently labeled molecules and consequently appear to lead to an overestimation of the *in vivo* K_d values relative to the *in vitro* K_d values (Fig. 1B, top). The overestimated K_d is also known as the "apparent K_d." Meanwhile, in the latter case, macromolecular crowding can occur because the cytosol contains numerous molecular species, such as proteins, lipids, and nucleotides, and so on, which occupy a substantial fraction of the volume within the cytoplasm (13). Such molecular crowding can profoundly influence protein-protein binding through an excluded-volume effect (14, 15) (Fig. 1B, bottom). The *in vivo* K_d confers a potential advantage to kinetic simulation models, because the *in vivo* K_d authentically includes the effects of all intracellular environments, such as competitive bindings and molecular crowding, on protein-protein interactions within a cell. However, to date, only a few *in vivo* K_d values have been made available for computer simulation for the EGFR-Ras-ERK MAP kinase pathway, possibly due to the technical difficulties.

FCCS allows the measurement of protein mobility, protein concentrations, and protein-protein interactions by exploiting the temporal fluorescence fluctuations of two diffusing fluorescently labeled particles under a confocal laser scanning microscope with a tiny focal volume, called the effective volume (16). As a distinct number of fluorescently labeled molecules diffuse through the effective volume (approximately 1 fl), the fluorescence signals fluctuate in a manner dependent on the mobility and concentration. An autocorrelation function of the fluctuating fluorescence signal provides the diffusion coefficient and concentration of molecules. FCCS utilizes two spectrally different fluorophores to label a pair of proteins. If the differently labeled particles are associated with each other, they pass through the effective volume in a synchronized way. Therefore, the simultaneous fluctuations of their fluorescence signals lead to an increase in the amplitude of the cross-correlation function. The amplitude provides the concentration of the protein-protein complex.

In this study, we established a method for obtaining *in vivo* K_d values in living cells by FCCS and determined >20 *in vivo* K_d values for the EGFR-Ras-ERK MAP kinase pathway in HeLa cells. In addition, we built a simulation model of the EGFR-Ras-ERK MAP kinase pathway based on the *in vivo* K_d values. This model suggested that multiple bindings of Shc to phosphorylated EGFR (pEGFR) are required for the peak activation of Ras, MEK, and ERK in response to EGF stimulation. Intriguingly, most of the *in vivo* K_d values measured in this study were higher than those measured previously by *in vitro* experiments, suggesting that competitive bindings play a major role in the *in vivo* K_d values within the cytoplasm.

MATERIALS AND METHODS

Plasmids. The cDNA of HaloTag was amplified by PCR using the pFC14A (HaloTag 7) cytomegalovirus (CMV) Flexi vector (Promega, Madison, WI) as the template. The cDNA of monomerized enhanced green fluorescent protein (mEGFP), HaloTag, or the GGSGGS linker was inserted into the pCAGGS, pCXN2, pCX4puro, or pCX4neo vector (17, 18) to generate pCAGGS-HaloTag-GGSGGS-mEGFP, pCAGGS-mEGFP, pCAGGS-FLAG-mEGFP, pCXN2-mEGFP, pCX4puro-HaloTag, pCX4neo-mEGFP, pCAGGS-FLAG-HaloTag, and pCXN2-HaloTag. pDONR223-RPS6KA1 (RSK1), pDONR223-RPS6KA2 (RSK3), and pDONR223-KSR (KSR1) were gifts from William Hahn (19) (Addgene plasmids 23860, 23530, and 23443, respectively). The cDNAs of human RSK1 and human RSK3 were amplified by PCR. The cDNAs of human Shc1 (20), human Grb2 (21), mouse Sos1 (22), mouse p85, cow p110α (23), human HRasdCT-G12V (where dCT stands for deleted C terminus) (24), human BRaf, human BRaf-S364A (25), human CRaf, human CRaf-S259A (24), human RSK2 (26), human RSK1, and human RSK3 were subcloned into mEGFP or HaloTag vector to generate pCXN2-mEGFP-Shc1-stop, pCX4puro-HaloTag-Shc, pCAGGS-FLAG-Grb2-HaloTag, pCAGGS-mEGFP-Sos1, pCAGGS-FLAG-p85-HaloTag, pCAGGS-mEGFP-p110α, pCXN2-HaloTag-HRasdCT-G12V, pCAGGS-

FLAG-BRaf-mEGFP, pCAGGS-FLAG-BRaf-S364A-mEGFP, pCAGGS-FLAG-CRaf-mEGFP, pCAGGS-FLAG-CRaf-S259A-mEGFP, pCXN2-HaloTag-RSK1, pCXN2-HaloTag-RSK2, and pCXN2-HaloTag-RSK3, respectively. Human MEK1, human MEK2, human ERK1, and human ERK2 were obtained by reverse transcription-PCR (RT-PCR) with a HeLa cDNA library and subcloned into the mEGFP or HaloTag vector to generate pCAGGS-FLAG-MEK1-HaloTag, pCAGGS-FLAG-MEK2-HaloTag, pCXN2-mEGFP-ERK1, and pCXN2-mEGFP-ERK2, respectively. The *ccdB* gene and chloramphenicol resistance genes sandwiched with aatR1 and aatR2 were amplified by PCR and inserted into the pCAGGS-mEGFP vector. pCAGGS-mEGFP-KSR1 was constructed with pCAGGS-mEGFP-ccdB and pDONR223-KSR by using the Gateway vector conversion system according to the manufacturer's instructions (Invitrogen, San Diego, CA). The cDNA of human EGFR was subcloned into the pPBbsr2-mEGFP vector to generate pPBbsr2-EGFR-mEGFP (27).

Cells, reagents, and antibodies. HeLa cells were purchased from the Human Science Research Resources Bank (Sennanshi, Japan) and maintained in Dulbecco's modified Eagle medium (DMEM) (Sigma-Aldrich, St. Louis, MO) supplemented with 10% fetal bovine serum (FBS). HeLa cells stably expressing mEGFP, HaloTag, or both HaloTag-Shc and EGFR-mEGFP were established in accordance with the conventional retroviral gene transfer and piggyBac transposon systems (17, 28). EGF and sodium orthovanadate (Na_3VO_4) were purchased from Sigma-Aldrich. Tetradecanoyl phorbol acetate (TPA) was purchased from Calbiochem (La Jolla, CA). HaloTag-TMR (tetramethylrhodamine) ligand and anti-HaloTag antibody (G9281) were purchased from Promega. The following antibodies were also used in this study: anti-Grb2 (catalog number sc-255), anti-RSK1 (catalog number sc-231), anti-RSK2 (catalog number sc-9986), and anti-RSK3 (catalog number sc-1431) antibodies (purchased from Santa Cruz Biotechnology, Santa Cruz, CA); anti-Shc (catalog number 610879), anti-MEK1 (catalog number 610121), and anti-MEK2 (catalog number 610235) antibodies (BD Transduction Laboratories, San Jose, CA); anti-green fluorescent protein (GFP) (catalog number 632375) antibody (Clontech, Palo Alto, CA); and anti-p44/p42 MAP kinase (ERK1/2) antibody (catalog number 4695; Cell Signaling Technology, Danvers, MA). PD-184352 was purchased from Toronto Research Chemicals (Toronto, Canada).

FCCS measurements. HeLa cells were plated onto 35-mm glass-base dishes (Asahi Techno Glass, Tokyo, Japan). One day after plating, plasmids were transfected by using 293fectin transfection reagent according to the manufacturer's instructions (Invitrogen, San Diego, CA). Two or three days after transfection, the cells were labeled with HaloTag-TMR ligand, as described below.

FCCS measurements were performed with the LSM780 Meta/ConfoCor 2 system (Carl Zeiss, Oberkochen, Germany) and the FV-1000 confocal imaging system (Olympus, Tokyo, Japan), equipped with gallium arsenide phosphide (GaAsP) detectors. With respect to the Zeiss system, the excitation lines were set at 488 nm and 561 nm. The excitation laser power under our microscopic settings was determined in accordance with a previous report (29). The excitation beam was reflected by an MBS 488/561 dichroic mirror and focused by a water immersion objective lens (C-Apochromat 40×/1.2 W Corr M27; Carl Zeiss). The emitted light was collimated and then split by an NFT 565 dichroic mirror. Emission signals were detected through a BP 505-540 infrared (IR) emission filter for mEGFP and a BP 615-680 IR emission filter for HaloTag-TMR. With respect to the Olympus system, the excitation lines were set at 488 nm and 559 nm. The excitation beam was reflected by a DM 405/488/559 dichroic mirror and focused by an oil immersion objective lens (60×/1.35-numerical-aperture [NA] Uplsapo 60XO; Olympus). The emitted light was detected through a diffraction grating to measure the fluorescence at wavelengths of 495 to 540 nm for mEGFP and 575 to 630 nm for HaloTag-TMR. FCCS measurements were performed for 28 s (Zeiss) and 17 s (Olympus) for each point and repeated at 7 different points per cell. At least 10 cells were examined under all conditions. All FCCS experiments were performed at room temperature.

Spectroscopy by confocal microscopy. HeLa cells were transfected with a plasmid encoding mEGFP- or HaloTag-fused proteins. Two days after transfection, the cells were incubated for 15 min with 5 μM HaloTag-TMR ligand at 37°C, washed twice with phosphate-buffered saline (PBS), and incubated for 30 min in DMEM lacking all vitamins (DMEM-V) (30) at 37°C. Before imaging, cells were washed twice and fed with DMEM-V. Fluorescence spectra were acquired by using an FV-1000 confocal imaging system (Olympus, Tokyo, Japan). The excitation line was set at 488 nm or 559 nm. The excitation beam was reflected by a DM 405/488/559 dichroic mirror and focused by an oil immersion objective lens (Uplsapo 60XO, 1.35 NA; Olympus). Emission signals were detected in the lambda scanning mode.

Calculation of the effective detection volume. The effective detection volume of the confocal laser scanning microscope, V_{eff}, is given by the following equation:

$$V_{\text{eff}} = \pi^{3/2} w_{xy}^2 w_z \tag{4}$$

where w_{xy} and w_z are the lateral and axial $1/e^2$ distances, respectively. These are calculated as

$$w_{xy}{}^2 = 4Dt \tag{5}$$

$$w_z = w_{xy} \times k \tag{6}$$

where D and t indicate the diffusion coefficient and the average time for detected molecules to diffuse out of this volume, respectively, and k is a structure parameter defined as $k = w_z/w_{xy}$. The D value of rhodamine 6G in water at room temperature was determined previously to be 280 $\mu m^2/s$ (31). The t and k values were obtained by fluorescence correlation spectroscopy (FCS) measurements with rhodamine 6G in water at room temperature and fitting of the autocorrelation curve using ZEN software (Carl Zeiss). Thus, w_{xy} and w_z were calculated to be 0.24 μm and 1.81 μm, respectively, and V_{eff} was determined to be 0.58 ± 0.20 fl under our experimental conditions.

Data analysis for FCCS. Fluorescent signals were analyzed as described previously (29, 32). The fluorescence autocorrelation function $G_{\text{auto}}(\tau)$, from the mEGFP and HaloTag-TMR channels, $G_G(\tau)$ and $G_H(\tau)$, respectively, and the fluorescence cross-correlation function, $G_{\text{cross}}(\tau)$, were calculated according to the normalized correlation function:

$$G(\tau) = \frac{\langle I_i(t) - \langle I_i(t)\rangle\rangle\langle I_j(t+\tau) - \langle I_j(t)\rangle\rangle}{\langle I_i(t)\rangle\langle I_j(t)\rangle} \tag{7}$$

where τ indicates the time delay; I_i is the fluorescence intensity of the mEGFP channel ($i = G$) or the HaloTag-TMR channel ($i = H$); the angle brackets denote the time average; and $G_G(\tau)$, $G_H(\tau)$, and $G_{\text{cross}}(\tau)$ denote the autocorrelation functions of mEGFP ($i = j = G$), HaloTag-TMR ($i = j = H$), and the cross-correlation function ($i = G$ or H; $j = H$ or G), respectively. The calculated $G(\tau)$ values were fitted to the following equation:

$$G(\tau) = \frac{G(0)}{\left[1 + (\tau/\tau_D)\right]\left[1 + k^{-2} \times (\tau/\tau_D)\right]^{\frac{1}{2}}} + G(\infty) \tag{8}$$

where τ_D, k, $G(0)$, and $G(\infty)$ indicate the correlation time, the structural parameter, the amplitude of the correlation curve, and the $G(\tau)$ value when a correlation functions under steady state, respectively. For fitting, we used the Excel Solver tool to obtain τ_D, $G(0)$, and $G(\infty)$. The concentrations of mEGFP ([$EGFP_{\text{total}}$]), HaloTag-TMR ([$\text{HaloTag}_{\text{total}}$]), and the complex ([Complex]) are given as

$$\left[\text{EGFP}_{\text{total}}\right] = \frac{1}{G_G(0)} \frac{1}{N_A} \frac{1}{V_{\text{eff}}} \tag{9}$$

$$\left[\text{Halo Tag}_{\text{total}}\right] = \frac{1}{G_H(0)} \frac{1}{N_A} \frac{1}{V_{\text{eff}}} \tag{10}$$

$$\left[\text{complex}\right] = \frac{G_{\text{cross}}(0)}{G_G(0) \times G_H(0)} \frac{1}{N_A} \frac{1}{V_{\text{eff}}} \tag{11}$$

where N_A corresponds to the Avogadro number and V_{eff} is the effective detection volume, determined as described above. The value obtained by

dividing the cross-correlation amplitude by one of the autocorrelation amplitudes, called the relative cross-correlation (RCC), provides a direct measure of the fraction of molecular binding, as follows (16):

$$\mathrm{RCC}_G = \frac{[\mathrm{Complex}]}{[\mathrm{EGFP}_{\mathrm{total}}]} = \frac{G_{\mathrm{cross}}(0)}{G_H(0)} \tag{12}$$

$$\mathrm{RCC}_H = \frac{[\mathrm{Complex}]}{[\mathrm{HaloTag}_{\mathrm{total}}]} = \frac{G_{\mathrm{cross}}(0)}{G_G(0)} \tag{13}$$

where RCC_G and RCC_H are the relative cross-correlations of EGFP and HaloTag, respectively. These RCC values were then corrected by the RCC values obtained from the positive control ($\mathrm{RCC}_{\mathrm{PC\_}G}$ and $\mathrm{RCC}_{\mathrm{PC\_}H}$), in which two fluorescent proteins were linked by a short peptide, and the negative control ($\mathrm{RCC}_{\mathrm{NC\_}G}$ and $\mathrm{RCC}_{\mathrm{NC\_}H}$), in which two fluorescent proteins were expressed separately and would not bind each other. Thus, the corrected complex concentration, [cComplex], was given as

$$[\mathrm{cComplex}] = [\mathrm{EGFP}_{\mathrm{total}}]\frac{\mathrm{RCC}_G - \mathrm{RCC}_{\mathrm{NC\_}G}}{\mathrm{RCC}_{\mathrm{PC\_}G} - \mathrm{RCC}_{\mathrm{NC\_}G}} \tag{14}$$

$$[\mathrm{cComplex}] = [\mathrm{HaloTag}_{\mathrm{total}}]\frac{\mathrm{RCC}_H - \mathrm{RCC}_{\mathrm{NC\_}H}}{\mathrm{RCC}_{\mathrm{PC\_}H} - \mathrm{RCC}_{\mathrm{NC\_}H}} \tag{15}$$

The values of $\mathrm{RCC}_{\mathrm{PC\_}G}$, $\mathrm{RCC}_{\mathrm{PC\_}H}$, $\mathrm{RCC}_{\mathrm{NC\_}G}$, and $\mathrm{RCC}_{\mathrm{NC\_}H}$ were measured in every experiment and used to obtain the [cComplex] value.

Calculation of *in vivo* K_d. According to the definition of K_d, the fraction of the complex in total EGFP or total HaloTag proteins is derived from equations 2, 14, and 15:

$$\frac{[\mathrm{cComplex}]}{[\mathrm{EGFP}_{\mathrm{total}}]} = \frac{[\mathrm{HaloTag}_{\mathrm{total}}] - [\mathrm{cComplex}]}{K_d + [\mathrm{HaloTag}_{\mathrm{total}}] - [\mathrm{cComplex}]} \tag{16}$$

$$\frac{[\mathrm{cComplex}]}{\mathrm{HaloTag}_{\mathrm{total}}} = \frac{[\mathrm{EGFP}_{\mathrm{total}}] - [\mathrm{cComplex}]}{K_d + [\mathrm{EGFP}_{\mathrm{total}}] - [\mathrm{cComplex}]} \tag{17}$$

The fractions of the bound protein in total EGFP and total HaloTag, i.e., the left-hand terms of equations 16 and 17, were plotted as a function of free (unbound) HaloTag and EGFP, respectively. The *in vivo* K_d value was obtained by nonlinear fitting of the experimental data with equations 16 and 17 and by averaging of these fitted values. For fitting, we used the Excel Solver function.

Quantification of concentrations of endogenous proteins in HeLa cells. The protein concentrations of endogenous Shc1, Grb2, MEK1, MEK2, ERK1, ERK2, RSK1, RSK2, and RSK3 in HeLa cells were determined as previously described (23). The 5myc-Flag-3HA-tagged (where HA stands for hemagglutinin) yellow fluorescent protein (YFP) and glutathione *S*-transferase (GST)-tagged HaloTag were purified from *Escherichia coli*. The lysates of the cells expressing mEGFP-Shc1, Grb2-mEGFP, MEK1-PAGFP, MEK2-m1YFP, mEGFP-ERK2, HaloTag-RSK1, HaloTag-RSK2, and HaloTag-RSK3 were used as references. The standard protein (10 ng, 5 ng, and 2.5 ng of 5myc-Flag-3HA-tagged YFP or GST-tagged HaloTag), the reference protein (a serial dilution of the reference lysate), and the total cell lysate obtained from 5.0×10^4, 2.5×10^4, or 1.25×10^4 cells were separated by SDS-PAGE, followed by immunoblotting with anti-GFP or anti-HaloTag antibodies (standard and reference) or specific antibodies (reference and total cell lysate). The bound antibodies were detected and quantified with an Odyssey infrared imaging system (Li-Cor). The amount of reference protein was determined by the relative intensity of the reference to 5myc-Flag-3HA-tagged YFP or GST-tagged HaloTag, and the amount of endogenous protein was calculated from the intensity of the reference protein. Finally, the concentration of endogenous protein in an individual HeLa cell was determined by dividing the amount of endogenous protein by the volume of a HeLa cell, which was 3.4×10^{-12} liters (9).

Kinetic modeling and numerical simulation. All kinetic reactions were described with mass action kinetics with CellDesigner (version 4.1) (33, 34) (see Fig. 6 and Tables 3 and 4.). Most of the enzymatic reactions were described as first-order reactions for simplicity. The reactions that follow the first-order enzymatic kinetics in our model (see Fig. 6) are as follows: Shc phosphorylation by EGFR (reaction 4), pShc dephosphorylation (reaction 5), Ras activation (reactions 11 and 12), Ras inactivation (reaction 13), Shoc2 activation by EGFR and inactivation (reaction 14), MEK phosphorylation by Raf (reaction 19), MEK dephosphorylation (reaction 20), and ERK dephosphorylation (reactions 26 to 29 and 38 to 41).

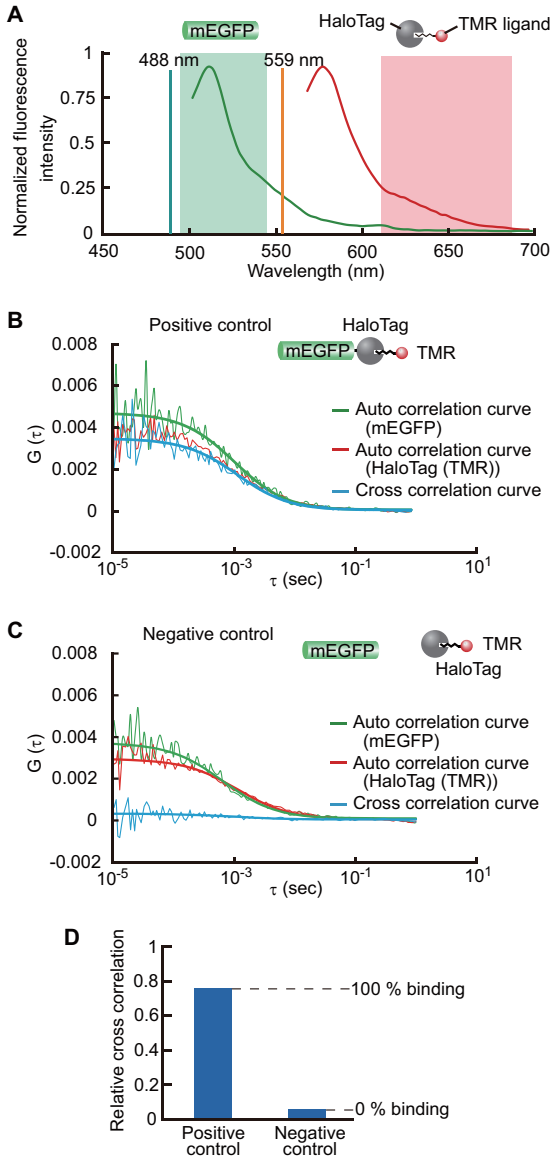

FIG 2 Experimental conditions for *in vivo* K_d measurement by FCCS. (A) Relative fluorescence emission spectra of mEGFP and HaloTag-TMR represented as a function of wavelength. Lines of 488 nm and 559 nm represent the excitation wavelengths for mEGFP and HaloTag-TMR, respectively. (B and C) HeLa cells expressing a fusion protein comprised of mEGFP, the GGSGGS linker, and HaloTag-TMR were subjected to FCCS measurement as a positive control (B). As a negative control (C), HeLa cells expressing individual mEGFP and HaloTag-TMR proteins were measured by FCCS. The autocorrelation curves for mEGFP and HaloTag-TMR and cross-correlation curves for the complex of the positive control and negative control are plotted as a function of the delay time, τ. Narrow and bold lines represent raw and fitted correlation curves, respectively. (D) The relative cross-correlation values for positive controls and negative controls are regarded as the values in the case of 100% binding and 0% binding, respectively. These values were measured at every experiment and used as reference values for correcting the fraction of the complex.

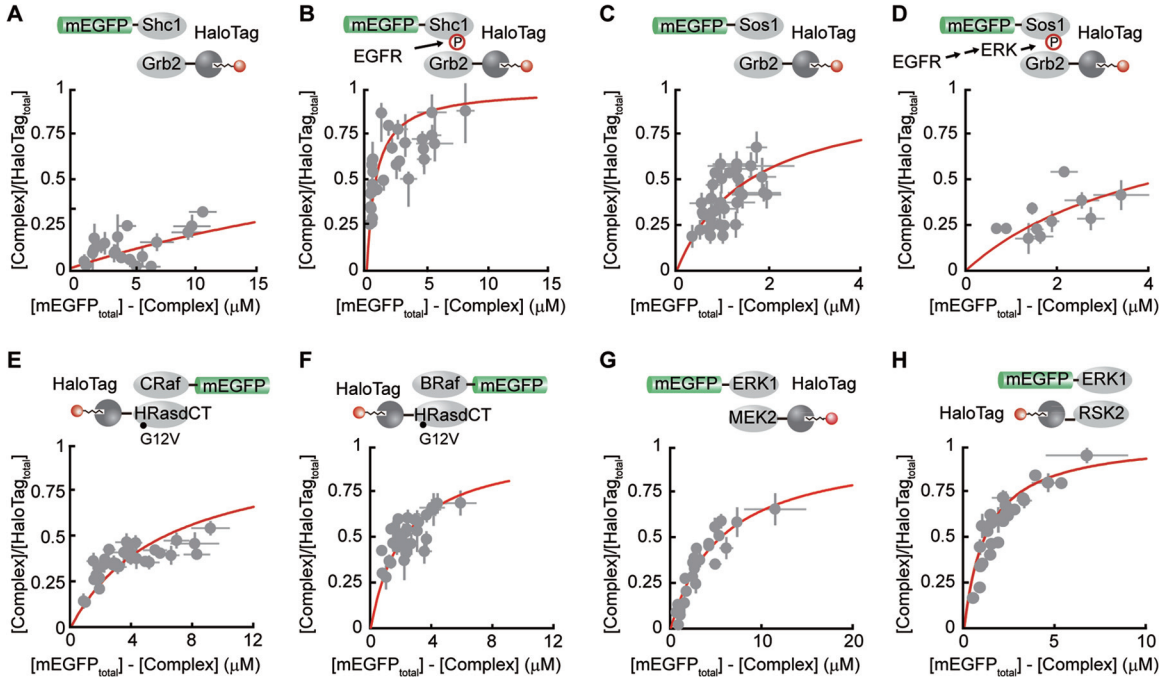

FIG 3 Measurement of *in vivo* K_d values for bindings of signaling molecules in the EGFR-Ras-ERK pathway. The measurements of the *in vivo* K_d values of the binding between Shc1-Grb2 (A and B), Grb2-Sos1 (C and D), HRasdCT-G12V–CRaf WT (E), HRasdCT-G12V–BRaf WT (F), MEK2-ERK1 (G), and ERK1-RSK2 (H) are shown. HeLa cells were transfected with plasmids expressing the indicated fusion proteins. Two or three days after transfection, the cells were treated with the TMR ligand, followed by serum starvation. The cells were then subjected to FCCS measurements. The fraction of the complex compared to the total HaloTag-TMR-fused proteins was plotted as a function of unbound mEGFP-fused proteins. EGF with Na_3VO_4 (B and D) was treated 30 min before FCCS measurements were started.

Among them, MEK dephosphorylation and ERK dephosphorylation were measured in our previous study (9, 22). The other reactions were approximated as first-order reactions for simplicity. The ordinary differential equations and parameters were exported to MATLAB software (version R2008b or R2010b; Mathworks Inc., Natick, MA) through Systems Biology Workbench (version 2.7.8) (35). Numerical simulation was performed by using the MATLAB function ode23, a numerical solver of differential equations for solving nonstiff problems. The simulation data calculated by ode23 did not differ from those obtained by ode15s, a numerical solver for stiff differential equations (data not shown). The concentrations of each isoform were summed to obtain the total concentrations. Dissociation constants of the summed proteins were weighted and summed as follows:

$$K_d = \frac{\sum_i^n \sum_j^m A_i B_j K_{d\,ij}}{\sum_i^n A_i \sum_j^m B_j} \quad (18)$$

where A_i and B_j correspond to the concentration of isoform i ($i = 1, 2, \ldots, m$) of protein A and the concentration of isoform j ($j = 1, 2, \ldots, n$) of protein B, respectively, and $K_{d\,ij}$ is the dissociation constant of the binding of A_i and B_j.

RESULTS

Strategy for measuring *in vivo* K_d. In this study, we attempted to measure the *in vivo* K_d between signaling proteins in the EGFR-Ras-ERK MAP kinase pathway with FCCS and to build a numerical model based on the experimentally verified parameters. Figure 1C provides a schematic of the procedure for measuring the *in vivo* K_d by FCCS. HeLa cells were cotransfected with two plasmids expressing chimeric proteins A and B, which were fused with different fluorescent proteins. Two or three days after transfection, we performed FCCS measurements at seven points in the cytoplasm of a single HeLa cell and obtained the concentrations of the fluorescently labeled molecules, [A_{total}] and [B_{total}], and their complex, [AB], from y intercepts, $G(0)$, of the auto- and cross-correlation curves, respectively (Fig. 1C). This analysis was repeated with at least 10 cells, and the fractions of [AB] to [B_{total}] were plotted as a function of [A_{total}] − [AB]. These plots were fitted to equations 16 and 17 to obtain the *in vivo* K_d value. It should be noted that this measurement requires the assumption of steady-state conditions, under which the binding reactions are in equilibrium kinetics.

Optimization of FCCS in HeLa cells. First, we examined which pairs of fluorescent proteins were most suited for the application of FCS/FCCS to living cells. In line with previous studies using GFP and red fluorescent protein (RFP) as a pair of fluorescent proteins for FCCS measurements (12, 36, 37), we tested the brightness, the degree of bleaching, and triplet formation. As reported previously, mEGFP exhibited sufficiently bright fluorescence, a small triplet fraction, and resistance to photobleaching. In contrast, substantial triplet fractions were detected in tdTomato and mCherry, as reported previously (38). Furthermore, Foo et al. reported previously that the low maturation efficiency of mCherry affected FCCS analysis (38).

To overcome the drawbacks of red fluorescent proteins in FCCS measurements, we took advantage of HaloTag, which is a modified haloalkane dehalogenase designed to covalently bind to synthetic ligands (HaloTag ligands) (39). The complex formed by conjugation of the HaloTag ligand to the membrane-permeable HaloTag-tetramethylrhodamine (TMR) ligand, here referred to

TABLE 1 Comparison of *in vivo* K_d values obtained in this study with *in vitro* K_d values measured previously by *in vitro* experiments[a]

	This study			Previous studies		
Binding	*In vivo* K_d (μM)	95% CI[b]	No. of measured cells	Mean *in vitro* K_d (μM) ± SD	Method[c]	Reference
Grb2-pShc				0.23 ± 55	SPR	61
	1.4[d]	0.7, 2.1	30	0.031 ± 8	SPR	61
				0.023	SPR	41
Grb2-Sos1	1.7	1.2, 2.2	23	0.001	Co-IP	62
	6.5[d]	3.3, 9.7	21	0.4	ITC	63
	2.8[e]	1.7, 3.9	18	21.4 ± 5.9	ITC	64
	2.1[f]	1.2, 1.5	16	1.7 ± 0.1	SPR	64
p110α-p85	<0.1		24	NR		
HRas-CRaf[g]	6.9	4.2, 9.6	34	0.12	ITC	65
	2.3[h]	1.7, 2.9	27	0.13	GDI assay	66
				0.0021	SPR	67
HRas-BRaf[f]	3.1	2.5, 3.7	33	0.0011	SPR	67
	3.5[i]	2.7, 4.3	28			
MEK1-ERK1	6.6	3.1, 10.1	22	0.058	Stopped flow	68
MEK1-ERK2				0.046–0.476	Michaelis constant	69
	11	7.2, 15	24	0.34 ± 0.06	Michaelis constant	70
				1.5	SPR	9
MEK2-ERK1	8.1	5.8, 10	24	NR		
MEK2-ERK2	5.6	3.8, 7.3	26	NR		
ERK1-RSK1	1.7	0.85, 2.5	22	NR		
ERK2-RSK1	0.87	0.54, 1.2	25	0.15 ± 0.01	SPR	71
ERK1-RSK2	2.1	1.5, 2.8	36	NR		
ERK2-RSK2	1.3	0.93, 1.7	36	NR		
ERK1-RSK3	1.0	0.51, 1.4	23	NR		
ERK2-RSK3	0.7	0.47, 0.91	27	NR		
MEK1-KSR1	1.5	0.99, 2.0	25	NR		
MEK1-KSR2	1.2	0.79, 1.6	23	NR		
MEK2-KSR1	1.3	0.77, 1.9	35	NR		
MEK2-KSR2	1.1	0.54, 1.6	22	NR		

[a] The *in vivo* K_d values quantified by FCCS in this study were compared with *in vitro* K_d values that were previously determined by *in vitro* experiments. NR, not reported.
[b] CI, confidence interval.
[c] SPR, surface plasmon resonance; co-IP, coimmunoprecipitation; ITC, isothermal calorimetry; GDI, guanine nucleotide dissociation inhibitor.
[d] In the presence of 10 ng/ml EGF and Na_3VO_4.
[e] In the presence of 1 mM TPA.
[f] In the presence of 10 μM PD-184352 (MEK inhibitor), 10 ng/ml EGF, and 10 mM Na_3VO_4.
[g] Carboxyl-terminus-deleted cytoplasmic HRas-G12V mutant.
[h] CRaf-S259A mutant.
[i] BRaf-S364A mutant.

as HaloTag-TMR, did not show detectable photobleaching or a detectable triplet fraction under these imaging conditions, indicating that this complex would have practical advantages for FCCS measurements. We acquired the fluorescence spectra of mEGFP and HaloTag-TMR in HeLa cells (Fig. 2A) and selected completely separable emission filters for mEGFP (505 to 540 nm) and HaloTag-TMR (615 to 680 nm).

We next performed FCCS by using a positive control and a negative control (Fig. 2B and C). A chimeric protein consisting of mEGFP, the GGSGGS linker, and HaloTag-TMR was used as a

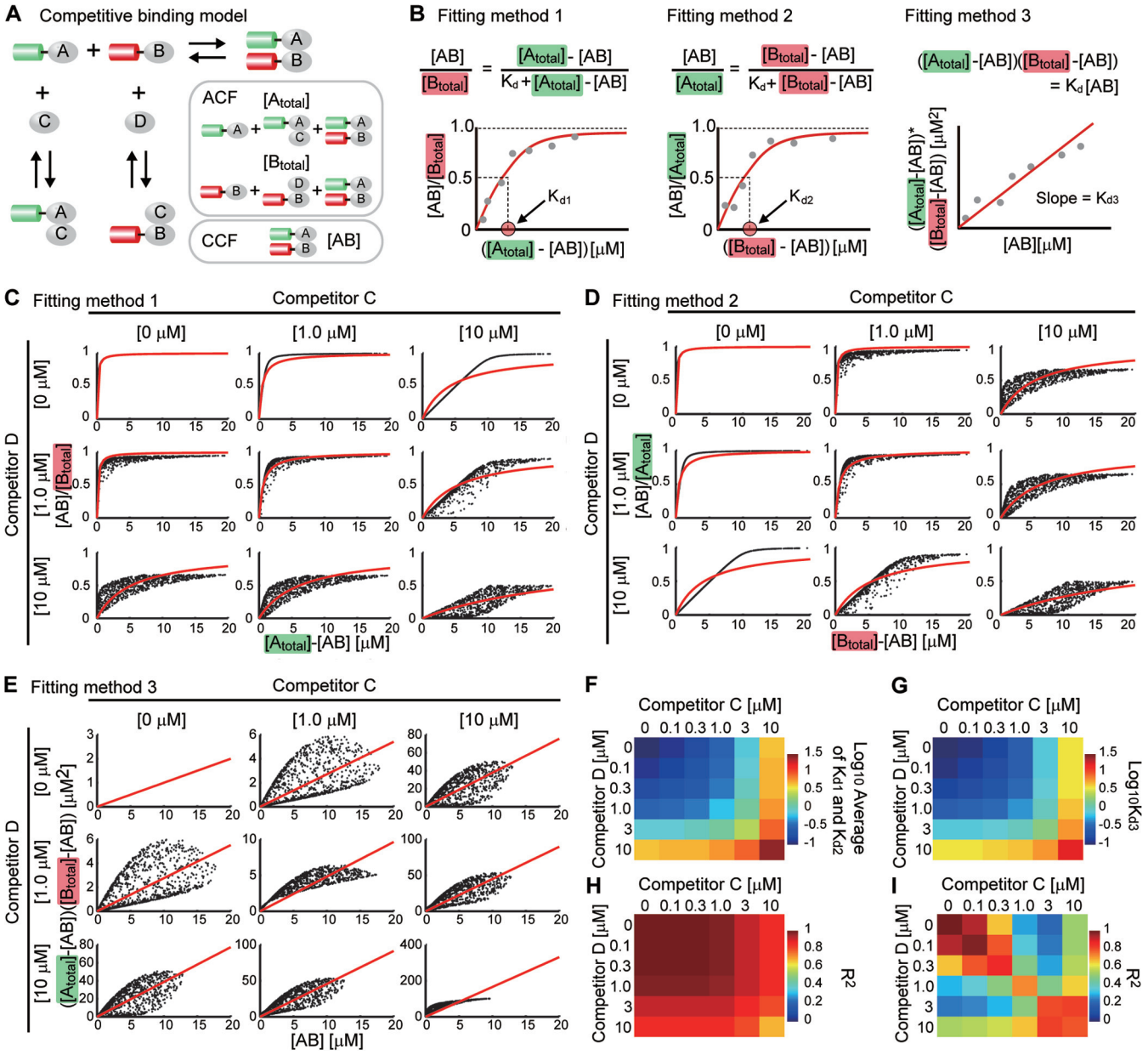

FIG 4 Computer simulation of the effects of endogenous competitors on measurements of *in vivo* K_d values. (A) Schematic competitive binding model. Green fluorescent protein-fused exogenous protein A binds to red fluorescent protein-fused exogenous protein B. Endogenous proteins C and D competitively bind to proteins A and B, respectively. Dissociation constants for all bindings in this model were assumed to be 0.1 μM. The species measured by the autocorrelation function (ACF) and cross-correlation function (CCF) are indicated in the insets. (B) Comparison among three fitting methods for *in vivo* K_d calculations. While fitting methods 1 and 2 were applied in this study, Foo et al. (38) previously employed fitting method 3. (C to E) The initial concentrations of proteins A and B were set randomly with a fixed concentration set of competitor proteins C and D. The concentrations of the AB protein complex, [AB], at steady state were calculated in accordance with the competitive binding model shown in panel A. Simulated results were plotted and fitted according to fitting method 1 (C), fitting method 2 (D), and fitting method 3 (E). Even though the concentrations of endogenous competitor proteins C and D were fixed values, the simulated plots varied widely from the fitting curves. (F and G) Heat maps showing the logarithmic *in vivo* K_d values obtained by averaging fitting methods 1 and 2 (F) and by fitting method 3 (K_{d3}) (G), with the indicated concentration set of competitor proteins C and D. (H and I) Heat maps showing the coefficient of determination (R^2) values obtained by averaging fitting methods 1 and 2 (H) and by fitting method 3 (I) with the indicated concentration sets of competitor proteins C and D. In several concentration sets of competitor proteins C and D, fitting methods 1 and 2 showed higher values for the coefficient of determination than those obtained by fitting method 3, indicating the advantage of the former method.

positive control. mEGFP and HaloTag expressed separately in cells were used as a negative control. We measured the autocorrelation functions of mEGFP (Fig. 2B and C, green lines) and HaloTag-TMR (red lines) and the cross-correlation function (blue lines). Ideally, with the positive-control sample, the *y* intercept of the autocorrelation function of GFP, $G_G(0)$, must be identical to that of HaloTag-TMR, $G_H(0)$, and also identical to the *y* intercept of the cross-correlation function, $G_{cross}(0)$. In the case of the negative-control sample, $G_{cross}(0)$ must be equal to 0. Thus, the relative cross-correlation (RCC) values, which represented the

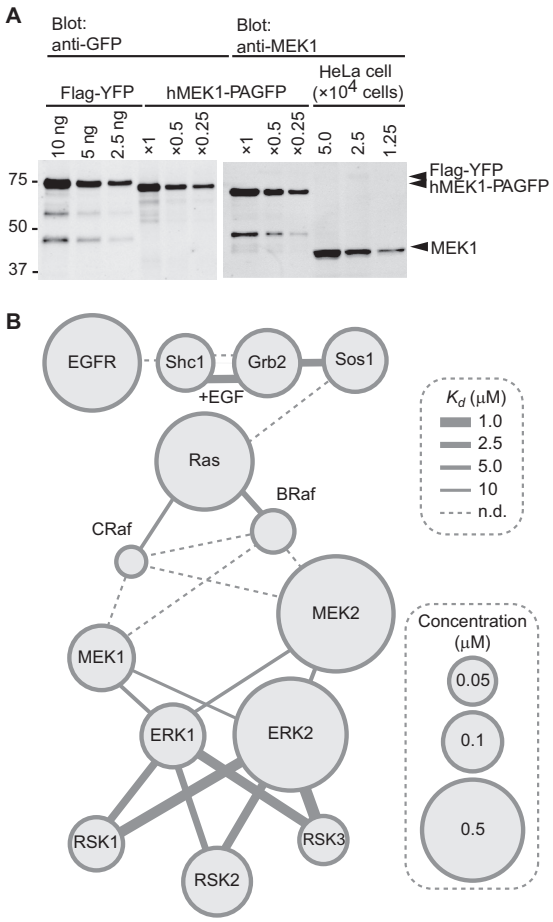

FIG 5 Quantitative map of the EGFR-Ras-ERK signaling pathway in a HeLa cell. (A) Protein concentrations of endogenous MEK1 in a HeLa cell were determined by quantitative Western blotting, as described in Materials and Methods. (B) Schematic representation of the *in vivo* K_d map of the EGFR-Ras-ERK pathway. The diameter of the circles represents the concentration of the indicated protein, and the line thickness indicates the *in vivo* K_d values in a HeLa cell.

fraction of the complex, theoretically must be 1 and 0 for the positive and negative controls, respectively. In our FCCS setup, the RCC values were within the range of 0.7 to 1.0 and 0.02 to 0.15 for the positive and negative controls, respectively (Fig. 2D). This deviation could be attributed to the imperfect overlap of the effective volumes of the two excitation lasers (38) and the spectral bleedthrough of EGFP fluorescence into the HaloTag-TMR emission channel. Therefore, we corrected the fraction of bound protein by using the RCC values of the positive and negative controls as 100% binding and 0% binding on each day of imaging, respectively (for more details, see Materials and Methods).

Measurement of *in vivo* K_d values of protein complexes in the EGFR-Ras-ERK MAP kinase pathway. By using the method described above, we quantified the *in vivo* K_d values of protein complexes that transmit signals in the EGFR-Ras-ERK MAP kinase pathway in living HeLa cells (Fig. 3 and see Table 2).

The adaptor protein Grb2 binds to another adaptor protein, Shc1, in a phosphotyrosine-dependent manner (40). In agreement with this property, the *in vivo* K_d value of the Grb2-Shc1 complex was >15 μM without growth factor stimulation (Fig. 3A). To maximize the tyrosine phosphorylation of Shc1, HeLa cells were stimulated with EGF in the presence of Na_3VO_4, a tyrosine phosphatase inhibitor. Under these conditions, the K_d value of the Grb2-Shc1 complex was 1.4 μM (Fig. 3B and Table 1). The *in vivo* K_d value was slightly higher than or comparable to those obtained *in vitro* (40, 41). Next, the K_d value of the Grb2-Sos1 complex mediated by the SH3 domain was determined to be approximately 1.7 μM (Fig. 3C and Table 1). The K_d was increased to 6.5 μM in EGF- and Na_3VO_3-treated cells (Fig. 3D and Table 1). This increase in the K_d was cancelled by the MEK inhibitor (Table 1). These data were consistent with the negative-feedback mechanism showing that Sos1 phosphorylation by ERK reduced the affinity of binding between Sos1 and Grb2 (42–44).

HRas localizes at the plasma membrane and Golgi apparatus via the lipid-modified C terminus (45, 46). We attempted to measure the binding between HRas-G12V, which was a constitutively active mutant, and CRaf. However, because of the slow diffusion of HRas at the plasma membrane, we failed to measure the *in vivo* K_d value for the binding of HRas-G12V to CRaf. To overcome this problem, we deleted the carboxyl terminus of HRas and prepared the cytoplasmic HRasdCT-G12V mutant (24). The K_d value of the HRasdCT-G12V–CRaf complex was 6.9 μM (Fig. 3E). Interestingly, the CRaf-S259A mutant, which adopts an open active conformation (24), bound to HRasdCT-G12V more strongly than did the CRaf wild type (WT), with an *in vivo* K_d of 2.3 μM (Table 1). In contrast, an equivalent mutation in BRaf, S364A, did not decrease the K_d value of the complex formed by HRasdCT-G12V and BRaf (Fig. 3F and Table 1), suggesting that the phosphorylation of BRaf at S364 plays a different role in Ras binding than the phosphorylation of CRaf at S259.

MEK has been shown to bind to and sequester ERK in the cytoplasm (47). ERK also binds to RSK through the D domain of the RSK LXL (DEJL) motif (48–50). There were also isoforms of them, MEK1, MEK2, ERK1, ERK2, RSK1, RSK2, and RSK3. We measured 10 possible combinations of the bindings among them (Fig. 3G and H and Table 1). We did not find any remarkable difference among the isoforms; therefore, the isoforms of MEK, ERK, and RSK were handled as single proteins in the simulation model described below.

The phosphatidylinositol 3-kinase (PI3-K) consists of a p85

TABLE 2 Concentrations of signaling molecules in the EGFR-Ras-ERK pathway in a HeLa cell[a]

Protein	No. of molecules/cell	Concn (μM)	Reference
EGFR		0.42	22
p46 Shc	1.4×10^5	0.068	This study
p52 Shc	1.7×10^5	0.083	This study
Grb2	2.9×10^5	0.14	This study
Sos1		0.12	22
Ras		0.43	51
BRaf	7.5×10^4	0.037	This study
CRaf		0.013	51
MEK1	2.6×10^5	0.13	This study
MEK2	1.5×10^6	0.74	This study
ERK1	2.4×10^5	0.12	This study
ERK2	1.4×10^6	0.68	This study
RSK1	1.5×10^5	0.073	This study
RSK2	3.1×10^5	0.15	This study
RSK3	1.1×10^5	0.054	This study

[a] Protein concentrations in a single HeLa cell were determined by dividing the number of molecules by a cell volume of 3.4 pl in a HeLa cell (9).

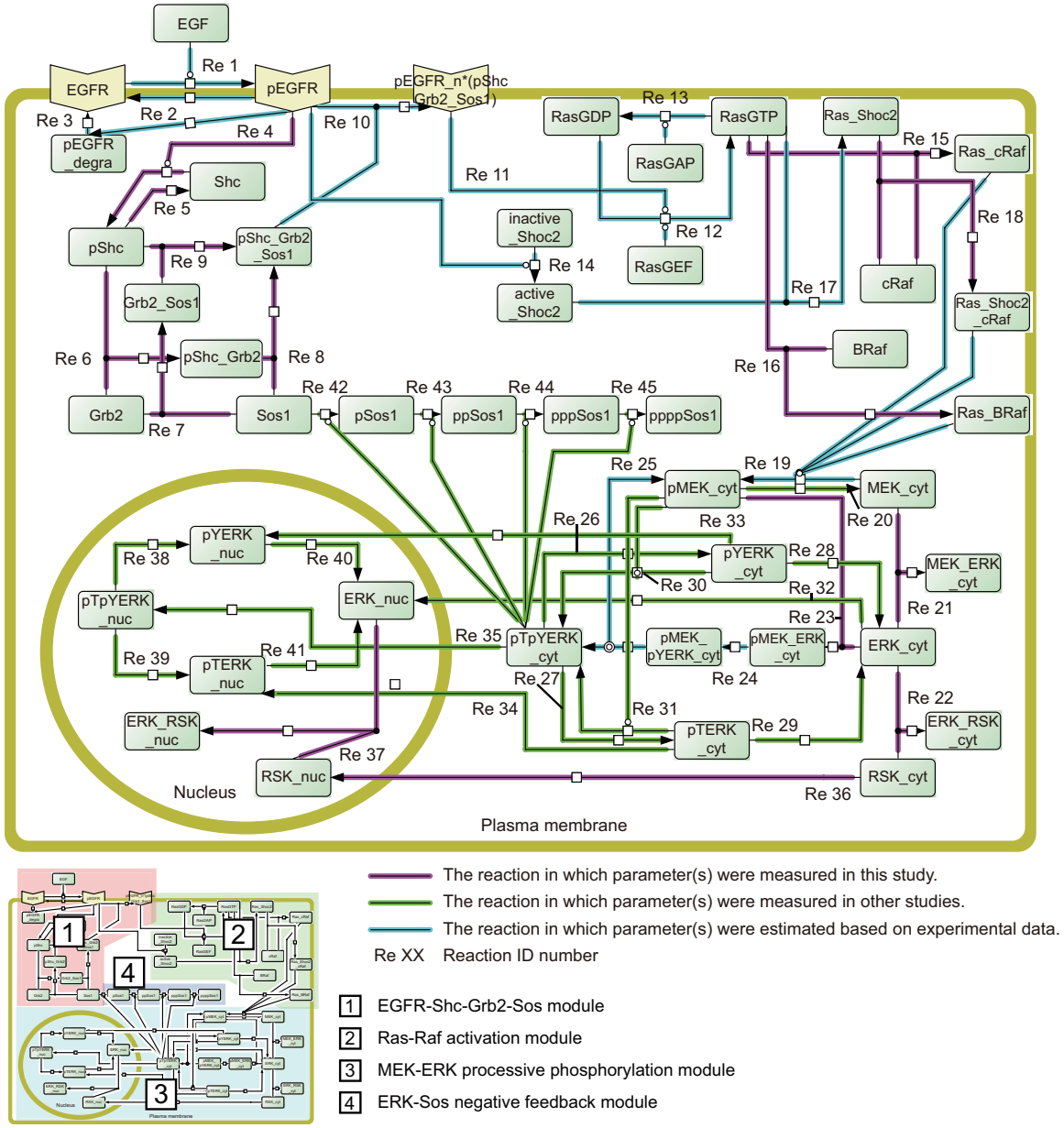

FIG 6 Kinetic simulation model of the EGFR-Ras-ERK MAP kinase pathway. The schematic of the EGFR-Ras-ERK pathway, which was created with CellDesigner (33), includes four modules: the EGFR-Shc-Grb2-Sos module (1), the Ras-Raf activation module (2), the MEK-ERK processive phosphorylation module (3), and the ERK-Sos negative-feedback module (4). The reaction identification (Re) number is indicated for each reaction. For more details, see Tables 3 and 4.

regulatory subunit and a p110 catalytic subunit. The K_d value of the PI3-K complex was <0.1 μM (Table 1). We could not precisely determine the K_d value by nonlinear curve fitting, because the lower detection limit of the concentration for mEGFP and HaloTag-TMR was ca. 0.1 μM under our experimental conditions.

Evaluation of the effects of competitive bindings on *in vivo* K_d values by computer simulation. Most of the *in vivo* K_d values obtained in this study were higher than the *in vitro* K_d values reported previously by an order of 1 or 2 (Table 1). This discrepancy strongly suggested that competitive binding had a greater effect on the *in vivo* K_d values than did molecular crowding. It should be noted that the large variability of each experimental plot from the fitting curve was caused by competitive binding. We simulated the effect of a fixed concentration of endogenous competitors on the *in vivo* K_d calculation by randomly changing the concentrations of two fluorescently labeled molecules (Fig. 4A and B). As expected, the *in vivo* K_d value was increased with the increase in the concentrations of endogenous competitors (Fig. 4C to E). The simulated plots were largely varied and dispersed, even though the concentrations of competitor proteins were fixed at constant values, as shown by the experimental data (Fig. 3). These simulation data were basically consistent with data reported in a previous study by Foo et al. (38). We compared fitting meth-

ods 1 and 2, which were used in this study, with fitting method 3, which was used in the study by Foo et al., and found that all of these methods provided almost the same *in vivo* K_d values (Fig. 4F and G). However, fitting methods 1 and 2 showed higher values for the coefficient of determination (R^2) between the fitting and simulation data than fitting method 3 (Fig. 4H and I). Therefore, we applied these fitting methods to the measurement of *in vivo* K_d values in this study.

Quantitative *in vivo* K_d map of the EGFR-Ras-ERK MAP kinase pathway. Quantitative Western blot analyses were used to measure the endogenous concentrations of proteins comprising the EGFR-Ras-ERK MAP kinase pathway in individual HeLa cells, including Shc, Grb2, MEK1, MEK2, ERK1, ERK2, RSK1, RSK2, and RSK3 (Fig. 5A and Table 2). These results, taken together with our previous data (22, 25, 51), are summarized in Table 2. Taking the *in vivo* K_d data (Table 1) and endogenous protein concentrations in a HeLa cell (Table 2) into account, we drew a quantitative interaction map of the EGFR-Ras-ERK MAP kinase pathway (Fig. 5B). In this scheme, the *in vivo* K_d values of Ras-CRaf and Ras-BRaf were the same as those of constitutively active Ras. Therefore, with the low abundance of Raf proteins, we speculated that signaling from Ras to Raf is the most inefficient part of the signal transduction pathway.

Model of the EGFR-Ras-ERK MAP kinase pathway. We built a simulation model of the EGFR-Ras-ERK MAP kinase pathway (Fig. 6 and Tables 3 and 4). This model was comprised of 4 modules, the EGFR-Shc-Grb2-Sos module, the Ras-Raf activation module (52), the MEK-ERK processive phosphorylation module (9), and the ERK-Sos1 negative-feedback module (22). EGFR was phosphorylated (pEGFR) upon EGF stimulation. Shc was phosphorylated by pEGFR, followed by binding to Grb2 and/or the Grb2-Sos complex. The pShc-Grb2-Sos ternary complex was associated with pEGFR. The bindings of Grb2 or the Grb2-Sos complex to pEGFR were ignored because we could not observe Grb2 binding to pEGFR in HeLa cells and A431 cells upon EGF stimulation (our unpublished observations), and we did not include the bindings of Shc, pShc, or pShc-Grb2 to pEGFR to avoid unnecessary complexity of the model.

The *in vivo* K_d values obtained in this study were used as the kinetic parameters to define 14 reactions in the model (Fig. 6, magenta lines), in addition to Shc phosphorylation/dephosphorylation rates (reactions 4 and 5) (Fig. 6 and 7A and B), the time course of EGFR and MEK phosphorylation upon EGF stimulation (Fig. 7C to E), and RSK1/RSK2/RSK3 nuclear import/export rates (reaction 36) (Fig. 6 and 7F and G). To constrain the parameters during simulation, we measured the stoichiometry of MEK phosphorylation by Phos-tag Western blotting (53) (Fig. 7H to K). Roughly 33% of MEK1/2 proteins were phosphorylated at Ser217/221 residues by Raf 10 min after EGF stimulation. Other kinetic parameters were either determined experimentally (Fig. 6, green lines) or estimated from experimental data from previous studies (22, 51) (Fig. 6, cyan lines).

Numerical simulation of the EGFR-Ras-ERK MAP kinase pathway based on *in vivo* K_d values. Numerical simulation of EGF-induced changes in the activity of EGFR (pEGFR), Ras (Ras-GTP), MEK (pMEK), and ERK (pTpY-ERK) in this original model demonstrated much lower values for Ras, MEK, and ERK than those obtained in experiments (Fig. 8A). This could be reasonable because *in vivo* K_d values obtained in this study were substantially higher than those used in the original models. We examined which reactions were rate-limiting steps and found three responsible reactions: from upstream, association of the pShc-Grb2-Sos complex with pEGFR (Fig. 8B, left), MEK phosphorylation by Raf (Fig. 8B, middle), and ERK phosphorylation by MEK (Fig. 8B, right). The latter two reactions were updated with the *in vivo* K_d values obtained in this study, resulting in decreases of the affinity of Ras-Raf binding and MEK-ERK binding, respectively. These reductions were corrected by multiplying the constant values, which approximately corresponded to the fold change in the reduction. Meanwhile, the detailed mechanisms of the association of the pShc-Grb2-Sos complex with pEGFR were not addressed, because we could not measure the dissociation constant of the reaction that took place at the plasma membrane.

TABLE 3 Initial concentrations of signaling molecules in simulations[a]

Protein	Concn (μM)	Description or reference
EGF	0.016	10 ng/ml
EGFR	0.42	22
Shoc2	0.67	72
Shc	0.15	This study
Grb2	0.14	This study
Sos1	0.12	22
Ras	0.43	51
BRaf	0.037	This study
CRaf	0.013	51
MEK	0.87	This study
ERK	0.79	This study
RSK	0.28	This study
RasGEF	1.0	22
RasGAP	1.0	22

[a] The initial concentrations of species in the simulation model are listed. The concentrations of isoforms, e.g., MEK1 and MEK2, are summed simply.

Role of multiple Shc bindings to pEGFR. To assess the role of pEGFR-Shc binding, we examined the dissociation constant and stoichiometry of binding by employing our quantitative simulation model. The phosphotyrosine binding (PTB) domain of Shc1 has been reported to interact with multiple sites of phosphorylated tyrosine residues of pEGFR. Jones et al. previously measured the dissociation constants of bindings between the Shc1 PTB domain and 6 phosphotyrosine residues of pEGFR by using protein microarrays. The *in vitro* K_d values were 0.040 μM for pY1172, 0.133 μM for pY1138, 0.317 μM for pY1192, 0.321 μM for pY1110, 0.628 μM for pY1016, and 1.152 μM for pY998 (54). To examine the role of these multiple binding sites, we numerically changed the parameters of binding between pEGFR and Shc, with ranges of 0.001 μM to 10 μM for the dissociation constant and 0 to 6 for stoichiometry, and calculated the residual sum square (RSS) values, which were a measure of how well the simulated data set fit with the experimental data. In Fig. 8C, blue represents a better fit to the experimental data. If a single binding site, namely, a stoichiometry value of 1, was assumed in the model, the best fit was obtained with a K_d value of 0.057 μM, which seemed to be implausible because this value was almost comparable to the lowest *in vitro* K_d value of pEGFR-Shc binding, 0.040 μM (54). Furthermore, the time courses of activation of Ras, MEK, and ERK were very dull under this condition (Fig. 8D). On the other hand, both the dissociation constant and stoichiometry were fitted to the experimental data, providing values of 0.250 μM and 5.9, respectively (Fig. 8C and E). We set the K_d value at 0.25 μM and examined the effect of stoichiometry on the time courses of activation

TABLE 4 Kinetic reactions and parameters[f]

Reaction identification	Reaction and equation	Parameter			
		Abbreviation	Value	Unit of measure	Description or reference
1	EGF + EGFR ⇔ pEGFR	k_f	100	μM/s	Estimated from Fig. 7
	$k_f \cdot$ EGF · EGFR − $k_b \cdot$ pEGFR	k_b	0.15	s	Estimated from Fig. 7
2	EGF_EGFR → pEGFR_degra	k_f	0.002	s	Estimated from Fig. 7
	$k_f \cdot$ pEGFR				
3	pEGFR_degra → EGFR	k_f	0.001	s	Estimated from Fig. 7
	$k_f \cdot$ pEGFR_degra				
4	Shc + **pEGFR** → pShc	k_f	0.031	μM/s	Quantified in Fig. 7[a]
	$k_f \cdot$ pEGFR · Shc				
5	pShc → Shc	k_f	0.028	s	Quantified in Fig. 7[a]
	$k_f \cdot$ pShc				
6	pShc + Grb2 ⇔ pShc_Grb2	k_f	0.1	μM/s	Calculated from *in vivo* K_d value[b]
	$k_f \cdot$ pShc · Grb2 − $k_b \cdot$ pShc_Grb2	k_b	0.14	s	
7	Grb2 + Sos1 ⇔ Grb2_Sos1	k_f	0.1	μM/s	Calculated from *in vivo* K_d value[b]
	$k_f \cdot$ Grb2 · Sos1 − $k_b \cdot$ Grb2_Sos1	k_b	0.17	s	
8	pShc_Grb2 + Sos1 ⇔ pShc_Grb2_Sos1	k_f	0.1	μM/s	Calculated from *in vivo* K_d value[b]
	$k_f \cdot$ pShc_Grb2 · Sos1 − $k_b \cdot$ pShc_Grb2_Sos1	k_b	0.17	s	
9	pShc + Grb2_Sos1 ⇔ pShc_Grb2_Sos1	k_f	0.1	μM/s	Calculated from *in vivo* K_d value[b]
	$k_f \cdot$ pShc · Grb2_Sos1 − $k_b \cdot$ pShc_Grb2_Sos1	k_b	0.14	s	
10	pEGFR + $n \cdot$ pShc_Grb2_Sos1 ⇔ pEGFR_(pShc_Grb2_Sos1)^n	k_f	0.1	μM/s	See text
	(pEGFR) $k_f \cdot$ pEGFR · pShc_Grb2_Sos1 − $k_b \cdot$ pEGFR_(pShc_Grb2_Sos1)^n	k_b	(0.1[c], 0.0056[d], 0.02[e])	s	
	[pShc_Grb2_Sos1) $n \cdot (k_f \cdot$ pEGFR · pShc_Grb2_Sos1 − $k_b \cdot$ pEGFR_(pShc_Grb2_Sos1)^n]	n	(1[c,d], 5.9[e])		
11	RasGDP + pEGFR_(pShc_Grb2_Sos1)^n (enzyme) → RasGTP	k_f	1	μM/s	73
	$k_f \cdot n \cdot$ pEGFR_(pShc_Grb2_Sos1)^n · RasGDP	n	(1[c,d], 5.9[e])		See text
12	RasGDP + **RasGEF** → RasGTP	k_f	0.00005	μM/s	22
	$k_f \cdot$ RasGEF · RasGDP				
13	RasGTP + **RasGAP** → RasGDP	k_f	0.05	μM/s	22
	$k_f \cdot$ RasGAP · RasGTP				
14	Inactive_Shoc2 + pEGFR (enzyme) ⇔ Active_Shoc2	k_f	0.1	μM/s	52
	$k_f \cdot$ inactive_Shoc2 · pEGFR − $k_b \cdot$ active_Shoc2	k_b	0.1	s	
15	RasGTP + cRaf ⇔ Ras_cRaf	k_f	0.1	μM/s	Calculated from *in vivo* K_d value[b]
	$k_f \cdot$ RasGTP · cRaf − $k_b \cdot$ Ras_cRaf	k_b	0.23	s	
16	RasGTP + BRaf ⇔ Ras_BRaf	k_f	0.1	μM/s	Calculated from *in vivo* K_d value[b]
	$k_f \cdot$ RasGTP · BRaf − $k_b \cdot$ Ras_BRaf	k_b	0.31	s	
17	RasGTP + active_Shoc2 ⇔ Ras_Shoc2	k_f	1	μM/s	52
	$k_f \cdot$ RasGTP · active_Shoc2 − $k_b \cdot$ Ras_Shoc2	k_b	0.1	s	

(Continued on following page)

TABLE 4 (Continued)

Reaction identification	Reaction and equation	Parameter			Description or reference
		Abbreviation	Value	Unit of measure	
18	Ras_Shoc2 + cRaf ⇔ Ras_Shoc2_cRaf	k_f	0.1	μM/s	Calculated from *in vivo* K_d value[b]
	$k_f \cdot$ Ras_Shoc2 · cRaf − $k_b \cdot$ Ras_Shoc2_cRaf	k_b	0.23	s	
19	MEK_cyt + **(Ras_cRaf + Ras_BRaf + Ras_Shoc2_cRaf)** → pMEK_cyt $k_f \cdot$ MEK_cyt · (Ras_cRaf + Ras_BRaf + Ras_Shoc2_cRaf)	k_f	(1[c], 10[d,e])	μM/s	See text
20	pMEK_cyt → MEK_cyt $k_f \cdot$ pMEK_cyt	k_f	0.0096	s	9
21	MEK_cyt + ERK_cyt ⇔ MEK_ERK_cyt	k_f	0.1	μM/s	Calculated from *in vivo* K_d value[b]
	$k_f \cdot$ MEK_cyt · ERK_cyt − $k_b \cdot$ MEK_ERK_cyt	k_b	0.66	s	
22	ERK_cyt + RSK_cyt ⇔ ERK_RSK_cyt	k_f	0.1	μM/s	Calculated from *in vivo* K_d value[b]
	$k_f \cdot$ ERK_cyt · RSK_cyt − $k_b \cdot$ ERK_RSK_cyt	k_b	0.12	s	
23	pMEK_cyt + ERK_cyt ⇔ pMEK_ERK_cyt	k_f	0.1	μM/s	Calculated from *in vivo* K_d value[b]
	$k_f \cdot$ pMEK_cyt · ERK_cyt − $k_b \cdot$ pMEK_ERK_cyt	k_b	0.66	s	
24	pMEK_ERK_cyt → pMEK_pYERK_cyt $k_f \cdot$ pMEK_ERK_cyt	k_f	(0.073[c], 0.32[d,e])	s	See text
25	pMEK_pYERK_cyt → pTpYERK_cyt + pMEK_cyt $k_f \cdot$ pMEK_pYERK_cyt	k_f	0.05	μM/s	9
26	pTpYERK_cyt → pYERK_cyt $k_f \cdot$ pTpYERK_cyt	k_f	0.004	μM/s	9
27	pTpYERK_cyt → pTERK_cyt $k_f \cdot$ pTpYERK_cyt	k_f	0.0055	μM/s	9
28	pYERK_cyt → ERK_cyt $k_f \cdot$ pYERK_cyt	k_f	0.0067	μM/s	9
29	pTERK_cyt → ERK_cyt $k_f \cdot$ pTERK_cyt	k_f	0.0068	μM/s	9
30	pYERK_cyt + **pMEK_cyt** → pTpYERK_cyt $k_f \cdot$ pYERK_cyt · pMEK_cyt	k_f	0.021	μM/s	9
31	pTERK_cyt + **pMEK_cyt** → pTpYERK_cyt $k_f \cdot$ pYERK_cyt · pMEK_cyt	k_f	0.02	μM/s	9
32	ERK_cyt ⇔ ERK_nuc $k_f \cdot$ ERK_cyt − $k_b \cdot$ ERK_nuc	k_f k_b	0.0017 0.013	s s	9
33	pYERK_cyt ⇔ pYERK_nuc $k_f \cdot$ pYERK_cyt − $k_b \cdot$ pYERK_nuc	k_f k_b	0.0025 0.017	s s	9
34	pTERK_cyt ⇔ pTERK_nuc $k_f \cdot$ pTERK_cyt − $k_b \cdot$ pTERK_nuc	k_f k_b	0.0022 0.049	s s	9
35	pTpYERK_cyt ⇔ pTpYERK_nuc $k_f \cdot$ pTpYERK_cyt − $k_b \cdot$ pTpYERK_nuc	k_f k_b	0.0082 0.0076	s s	9

(Continued on following page)

TABLE 4 (Continued)

Reaction identification	Reaction and equation	Parameter			Description or reference
		Abbreviation	Value	Unit of measure	
36	RSK_cyt ⇔ RSK_nuc	k_f	0.001	s	Quantified in Fig. 7F and G
	$k_f \cdot$ RSK_cyt − $k_b \cdot$ RSK_nuc	k_b	0.11	s	Data not shown
37	ERK_nuc + RSK_nuc ⇔ ERK_RSK_nuc	k_f	0.1	μM/s	Calculated from *in vivo* K_d value[b]
	$k_f \cdot$ ERK_nuc $\cdot$ RSK_nuc − $k_b \cdot$ ERK_RSK_nuc	k_b	0.12	s	
38	pTpYERK_nuc → pYERK_nuc $k_f \cdot$ pTpYERK_nuc	k_f	0.0032	s	9
39	pTpYERK_nuc → pTERK_nuc $k_f \cdot$ pTpYERK_nuc	k_f	0.0038	s	9
40	pYERK_ nuc → ERK_nuc $k_f \cdot$ pYERK_nuc	k_f	0.0077	s	9
41	pTERK_ nuc → ERK_nuc $k_f \cdot$ pTERK_nuc	k_f	0.0058	s	9
42	Sos1 + **pTpYERK_cyt** ⇔ pSos1 $k_{cat} \cdot$ pTpYERK_cyt $\cdot$ Sos1/(K_m + Sos1) − $k_b \cdot$ pSos1	k_{cat} K_m k_b	0.02 1 0.0025	μM/s M s	22
43	pSos1 + **pTpYERK_cyt** ⇔ ppSos1 $k_{cat} \cdot$ pTpYERK_cyt $\cdot$ pSos1/(K_m + pSos1) − $k_b \cdot$ ppSos1	k_{cat} K_m k_b	0.02 1 0.0025	μM/s μM s	22
44	ppSos1 + **pTpYERK_cyt** ⇔ pppSos1 $k_{cat} \cdot$ pTpYERK_cyt $\cdot$ ppSos1/(K_m + ppSos1) − $k_b \cdot$ pppSos1	k_{cat} K_m k_b	0.02 1 0.0025	μM/s M s	22
45	pppSos1 + **pTpYERK_cyt** ⇔ ppppSos1 $k_{cat} \cdot$ pTpYERK_cyt $\cdot$ pppSos1/(k_m + pppSos1) − $k_b \cdot$ ppppSos1	k_{cat} K_m k_b	0.02 1 0.0025	μM/s μM s	22

[a] The enzymatic reaction was treated as a first-order enzymatic reaction.
[b] The k_f value was set to 0.1 mM/s. The k_b value was calculated from the k_f and *in vivo* K_d values obtained in this study (Table 1).
[c] The value is used in Fig. 8A.
[d] The value is used in Fig. 8D.
[e] The value is used in Fig. 8E.
[f] Reaction identification numbers correspond to the numbers in Fig. 6. Boldface type denotes enzymes.

of Ras, MEK, and ERK. We found that high stoichiometry is essential to recapitulate the peak activations of Ras, MEK, and ERK (Fig. 8E).

The prediction by the simulation model urged us to confirm experimentally the stoichiometry of Shc binding to EGFR. For this, we first established two stable HeLa cell lines expressing mEGFP or HaloTag, which were used to calibrate the concentrations of mEGFP and HaloTag by FCS. Next, HeLa cells stably expressing both EGFR-mEGFP and HaloTag-Shc were stimulated with EGF for 15 min to induce accumulation of EGFR-mEGFP and HaloTag-Shc on the endosomes (Fig. 8F and G). The concentration ratio of EGFR-mEGFP to HaloTag-Shc was determined on each endosome and plotted in a histogram (Fig. 8H). We found that approximately 3 Shc molecules associated with EGFR at endosomes upon EGF stimulation.

DISCUSSION

In this study, we established a method for obtaining the *in vivo* K_d in living cells by FCCS and used this method to determine 22 *in vivo* K_d values for the EGFR-Ras-ERK MAP kinase pathway. By combining these *in vivo* K_d values with intracellular concentrations quantified by Western blotting, we built a simulation model of this signaling pathway. This model indicated the possible effect of multivalent binding of Shc proteins to pEGFR on sufficient peak activations of Ras, MEK, and ERK. Therefore, to the best of our knowledge, this study is the first to show the essential role played by multiple Shc bindings to pEGFR in the EGFR signaling pathway. These results clearly demonstrate the validity of this method and quantitative simulation model. However, there are substantial discrepancies between the experimental and simulated results, especially for the transient peak activity and sustained

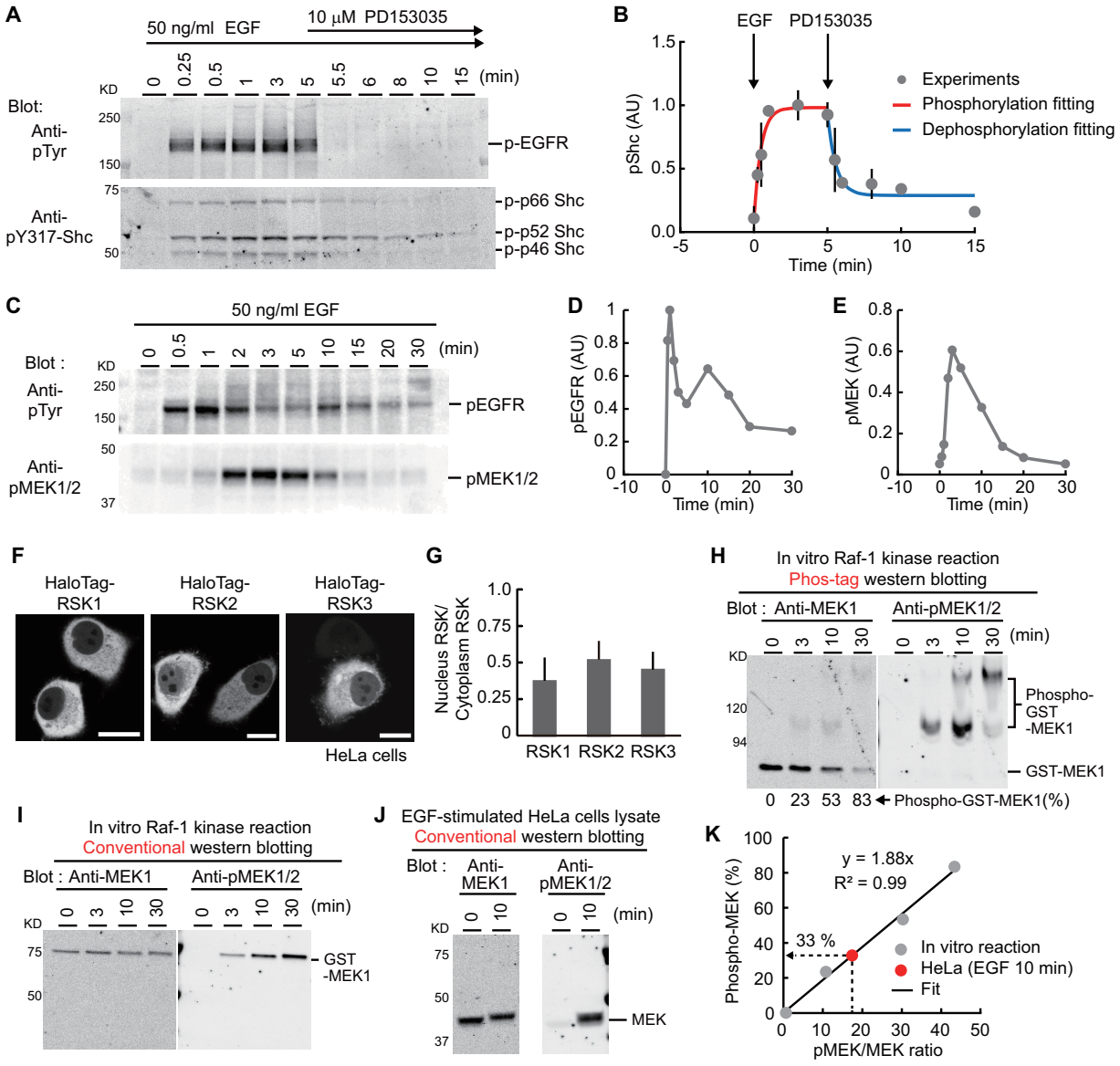

FIG 7 Quantifications of kinetic parameters for EGFR-Ras-ERK signaling. (A and B) Shc1 phosphorylation and dephosphorylation rates (reactions 4 and 5) (Fig. 6). Serum-starved HeLa cells were treated with 50 ng/ml EGF, followed by the addition of an EGFR inhibitor, 10 μM PD-153035, 5 min later. Cell lysates were subjected to Western blotting with antiphosphotyrosine and anti-pY317-Shc antibodies. Representative results of three independent experiments are shown (A). Averaged pShc intensity values were plotted as a function of time, with standard deviations (B). First, the pShc dephosphorylation rate constant was measured by fitting the experimental data with a single exponential function (blue line). The time constant of the fitted exponential function corresponds to the pShc dephosphorylation rate constant. Second, the Shc phosphorylation rate constant was calculated as follows. The time constant of phosphorylation was obtained by fitting the experimental data with a single exponential function (red line). The time constant value was subtracted from the pShc dephosphorylation rate constant and then divided by the EGFR concentration, providing the Shc phosphorylation rate by pEGFR. AU, arbitrary units. (C to E) Time courses of EGF-induced phosphorylation of EGFR and MEK1/2 in HeLa cells were examined by Western blotting (C) and quantified by densitometry (D and E). (F and G) Nuclear import and export rates of RSK1, RSK2, and RSK3 proteins. HeLa cells expressing HaloTag-fused RSK1, RSK2, or RSK3 were treated with the TMR ligand, followed by confocal microscopy (F), and the ratio of fluorescence intensity in the nucleus to that in the cytoplasm was quantified (G). The concentration ratio is equal to the ratio of the nuclear import rate to the nuclear export rate. Therefore, we set the nuclear import rate at 0.001/s, and the nuclear export rates were calculated by the ratio of nuclear intensity to cytoplasmic intensity. Bar, 15 μm. (H to K) Stoichiometry of phosphorylated MEK. Recombinant GST-MEK1 protein was phosphorylated *in vitro* by constitutively active CRaf kinase for the indicated time periods. The eluates were subjected to Phos-tag Western blotting. The fraction of phospho-GST-MEK1 was measured by the reduction of nonphosphorylated GST-MEK1 (H, left). The same eluates were also subjected to conventional Western blotting (I). The fractions of phosphorylated MEK1 were plotted as a function of the pMEK/MEK ratio and fitted with a linear function (K). EGF-stimulated HeLa cell lysates were analyzed by conventional Western blotting (J), and the fraction of phosphorylated MEK1/2 was calculated by using the reference function obtained in panel K.

basal activity of MEK and ERK upon EGF stimulation (Fig. 8E), suggesting the existence of other possible regulations to be addressed in the future.

The *in vivo* K_d is influenced by both competitive binding by a number of proteins and molecular crowding (Fig. 1B). Competitive bindings increase the *in vivo* K_d value, whereas molecular crowding decreases the *in vivo* K_d value through the excluded-volume effect in general (14, 15). Intriguingly, almost all of the *in*

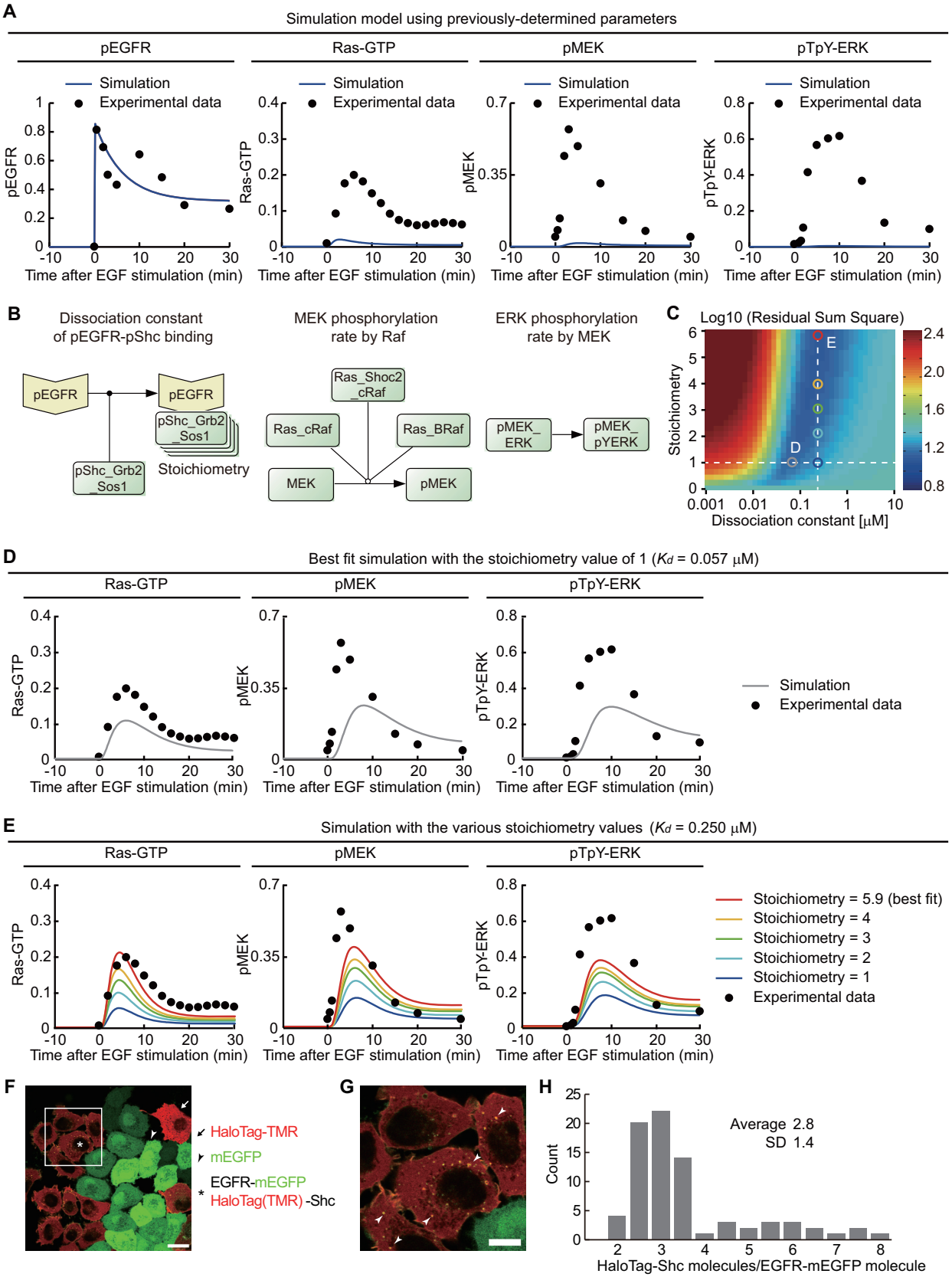

vivo K_d values determined in this study were higher than those measured previously in *in vitro* assays (Table 1). These findings suggested that competitive bindings, rather than molecular crowding, made a more significant contribution to *in vivo* K_d values. Of note, we could not exclude other potential explanations for the increased *in vivo* K_d values, such as changes in conformation and molecular crowding, under certain circumstances. Foo et al. reported previously that the *in vivo* K_d values of Cdc42 and its effectors could become close to the *in vitro* K_d values by introducing correcting factors, such as the maturation efficiency of fluorescent proteins, photobleaching, and fluorescence resonance energy transfer (FRET) (38). The application of these corrections to our data might lead to an improvement in the discrepancies between the *in vivo* and *in vitro* K_d values to some extent. However, the increase in *in vivo* K_d values is unavoidable and remarkable in the binding of a protein containing multiple domains for protein-protein bindings, such as adaptor molecules. Although we could not entirely exclude the possibility that other factors such as ionic strength alter K_d values, *in vivo* K_d values have a potential advantage to directly demonstrate how much proteins form complexes in living cells.

The quantitative *in vivo* K_d measurements clarified several regulatory mechanisms underlying the EGFR-Ras-ERK pathway. Research groups have studied the role of growth factor-induced Sos1 phosphorylation but have not reached the same conclusion. Sos1 has at least 4 serine residues phosphorylated mainly by ERK in the C-terminal domain, resulting in negative regulation of Sos1 as a Ras activator. Two regulatory mechanisms have been suggested for the phosphorylation-mediated negative regulation of Sos1: a phosphorylation-induced disassembly of the Grb2-Sos1 complex (42, 43) and a phosphorylation-induced dissociation of the Grb2-Sos1 complex from the activated EGF receptors (40, 55). However, most of those experiments were performed under *in vitro* conditions. Our results revealed that pretreatment with TPA or EGF and Na_3VO_4 increased the *in vivo* K_d value of the Grb2-Sos1 complex (Fig. 3C and D and Table 1), supporting the former mechanisms for negative feedback from ERK to Sos1. In addition, we found that HRasdCT-V12 bound preferentially to the CRaf-S259A mutant rather than to the CRaf WT (Fig. 3E and Table 1). This result agreed with previously reported findings showing a sequential state transition model of CRaf for its Ras binding; CRaf phosphorylated on Ser259 adopts a closed inactive conformation, and dephosphorylation of Ser259 induces CRaf to adopt a semi-closed inactive state to associate with Ras-GTP (24). In contrast, the *in vivo* K_d values for HRas binding to the BRaf WT and the BRaf-S364A mutant, which corresponded to the CRaf-S259A mutant, did not show any difference (Table 1). These results indicated a clear difference between Ras-CRaf WT binding and Ras–CRaf-S259A binding but not between Ras-BRaf WT and Ras–BRaf-S364A binding (Fig. 3 and Table 1). It has been well characterized that 14-3-3 binds to the CRaf S259 phosphorylation site to form a closed inactive state (24), and the BRaf S364 phosphorylation site is thought to be equivalent to the CRaf S259 phosphorylation site. We suggest that the CRaf S259 site is highly phosphorylated even in the basal state, and therefore, most CRaf WT proteins form a closed state, while the BRaf S364 site is not sufficiently phosphorylated, and therefore, a substantial amount of BRaf WT proteins form an open state. The other possibility is that another phosphoserine residue serves as the 14-3-3 binding site in BRaf (25). Notably, for technical reasons, we had to omit some important regulatory mechanisms. For example, *in vitro* analyses of CRaf-lipid interactions have revealed two distinct phospholipid binding regions within CRaf, at amino acid residues 139 to 184 and 390 to 423, for phosphatidylserine and phosphatidic acid, respectively (56, 57). These two regions function to promote translocation of CRaf to the membrane and to increase the affinity for GTP-Ras. Therefore, we might have overestimated *in vivo* K_d values of Ras-Raf binding, which was measured only in the cytoplasm. Even with this kind of limitation, we believe that measurements of *in vivo* K_d values by FCCS will provide compelling quantitative data for interactions in living cells.

We improved and optimized some of the experimental conditions of FCCS for our *in vivo* K_d measurements. EGFP and mCherry have hitherto been utilized as a fluorescent protein pair for FCCS measurements (12, 36, 37). However, the mCherry protein has been reported to exhibit slower chromophore maturation, a much greater triplet component, weaker photostability than the EGFP protein, and, consequently, a decrease in the signal-to-noise ratio of FCCS measurements (38). We found that HaloTag-TMR overcame all these flaws. The membrane-permeable TMR ligand needs to be added after HaloTag expression in cells. Based on the positive-control data, almost all HaloTag proteins were covalently attached to the TMR ligand (Fig. 2B), and the amount of free TMR ligand in the medium was negligible after the medium change. Further improvements will be needed to overcome the following limitations in our system. First, there is a limitation associated with the measurement of the *in vivo* K_d value for binding on the membrane. As we mentioned above, FCCS measurements of HRas and Raf binding on the membrane did not provide accurate and reproducible results, possibly because of the low diffusion constant, heterogeneous membrane structure, and leakage of the fluorescence signal of Raf from the cytoplasm. Sec-

FIG 8 Effect of multivalent binding of Shc1 to pEGFR on EGFR-Ras-ERK signaling. (A) EGF-induced kinetics of phospho-EGFR (pEGFR), Ras-GTP, phospho-MEK (pMEK), and phospho-ERK (pERK) were simulated in the models according to data shown in Fig. 6, without any corrections, and showed low signal transmission from Ras-GTP in comparison to the experimental data. The experimental time courses of Ras-GTP and pTpY-ERK were obtained in our previous studies (9, 22). The time courses of pEGFR and pMEK were quantified in this study (Fig. 7). (B) Three reactions involved in rate-limiting steps are shown. (C) Heat map representing the logarithmic residual sum square values between the experiments and numerical simulations, which varied with respect to both the dissociation constant and stoichiometry values of the reaction for Shc1-pEGFR binding. Blue indicates a better fit of the simulation to experiments. D and E indicate parameter sets used in panels D and E (best fit), respectively. (D) After parameter corrections for MEK phosphorylation (B, middle) and ERK phosphorylation (B, right), the EGF-induced kinetics of Ras-GTP, pMEK, and pERK were calculated with a stoichiometry value of 1.0 and fitted to experiments by changing the dissociation constant value (B, left). The best-fit dissociation constant was 0.057 μM. (E) EGF-induced kinetics of Ras-GTP, pMEK, and pERK were calculated with a dissociation constant of 0.25 μM and the indicated stoichiometry values. (F to H) Multiple bindings of Shc to pEGFR. HeLa cells expressing mEGFP, HaloTag, or both EGFR-mEGFP and HaloTag-Shc were cocultured at equal ratios. The boxed region in panel F is magnified in panel G. After incubation with the TMR ligand and serum starvation for 1 h, the cells were stimulated with 10 ng/ml EGF for 15 min, followed by fixation. By FCS, the concentrations of mEGFP and HaloTag-TMR were determined to be 2.5 μM and 12 μM, respectively. These values were used to calculate the ratio of HaloTag-Shc to EGFR-mEGFP at each endosome in panel H ($n = 78$ endosomes from 28 cells). Bars, 20 μm (F) and 10 μm (G).

ond, the lower limit for the measurements of the *in vivo* K_d is also problematic. In our experimental setup, we could not reproducibly calculate the *in vivo* K_d at values of <0.1 μM. This was due mainly to the sensitivity of fluorescence detection by imaging of cells with low EGFP and HaloTag-TMR expression levels, in which autofluorescence and substantial photobleaching interfered with data acquisition. The third limitation concerns the measurement of the *in vivo* K_d values in ternary protein complexes. There are many scaffold proteins in the EGFR-Ras-ERK MAP kinase pathway that regulate signaling efficiency and specificity (58–60). Measurements of the *in vivo* K_d values in ternary protein complexes by FCCS will shed new light on how these scaffold proteins regulate efficiency, specificity, and divergence in the signaling pathway more quantitatively.

We established a method for measuring the *in vivo* K_d in living cells by FCCS and quantified >20 *in vivo* K_d values for protein-protein interactions involved in the EGFR-Ras-ERK MAP kinase pathway in living HeLa cells. These *in vivo* K_d values provide quantitative data that will help to elucidate various signaling pathways.

ACKNOWLEDGMENTS

We thank Kazunari Kaizu and Koichi Takahasi (QBiC, Japan) and the members of the Matsuda Laboratory for helpful discussions. We are also grateful to the Center for Meso-Bio Single Molecule Imaging and the Institute for Integrated Cell-Material Sciences at Kyoto University for the use of the microscope.

K.A. and M.M. were supported by the Research Program of Innovative Cell Biology by Innovative Technology (Cell Innovation) and the Platform for Dynamic Approaches to Living System from the Ministry of Education, Culture, Sports, and Science, Japan. K.A. was supported by the JST PRESTO program and by JSPS KAKENHI (23136504 and 25136706). W.S. was supported by the Yoshida Scholarship Foundation.

REFERENCES

1. **Chang L, Karin M.** 2001. Mammalian MAP kinase signalling cascades. Nature **410:**37–40. http://dx.doi.org/10.1038/35065000.
2. **Chen Z, Gibson TB, Robinson F, Silvestro L, Pearson G, Xu B, Wright A, Vanderbilt C, Cobb MH.** 2001. MAP kinases. Chem. Rev. **101:**2449–2476. http://dx.doi.org/10.1021/cr000241p.
3. **Qi M, Elion EA.** 2005. MAP kinase pathways. J. Cell Sci. **118:**3569–3572. http://dx.doi.org/10.1242/jcs.02470.
4. **Bhalla US, Ram PT, Iyengar R.** 2002. MAP kinase phosphatase as a locus of flexibility in a mitogen-activated protein kinase signaling network. Science **297:**1018–1023. http://dx.doi.org/10.1126/science.1068873.
5. **Nakakuki T, Birtwistle MR, Saeki Y, Yumoto N, Ide K, Nagashima T, Brusch L, Ogunnaike BA, Okada-Hatakeyama M, Kholodenko BN.** 2010. Ligand-specific c-Fos expression emerges from the spatiotemporal control of ErbB network dynamics. Cell **141:**884–896. http://dx.doi.org/10.1016/j.cell.2010.03.054.
6. **Sasagawa S, Ozaki Y, Fujita K, Kuroda S.** 2005. Prediction and validation of the distinct dynamics of transient and sustained ERK activation. Nat. Cell Biol. **7:**365–373. http://dx.doi.org/10.1038/ncb1233.
7. **Schoeberl B, Eichler-Jonsson C, Gilles ED, Muller G.** 2002. Computational modeling of the dynamics of the MAP kinase cascade activated by surface and internalized EGF receptors. Nat. Biotechnol. **20:**370–375. http://dx.doi.org/10.1038/nbt0402-370.
8. **Bandyopadhyay S, Chiang CY, Srivastava J, Gersten M, White S, Bell R, Kurschner C, Martin C, Smoot M, Sahasrabudhe S, Barber DL, Chanda SK, Ideker T.** 2010. A human MAP kinase interactome. Nat. Methods **7:**801–805. http://dx.doi.org/10.1038/nmeth.1506.
9. **Aoki K, Yamada M, Kunida K, Yasuda S, Matsuda M.** 2011. Processive phosphorylation of ERK MAP kinase in mammalian cells. Proc. Natl. Acad. Sci. U. S. A. **108:**12675–12680. http://dx.doi.org/10.1073/pnas.1104030108.
10. **Kasai RS, Suzuki KG, Prossnitz ER, Koyama-Honda I, Nakada C, Fujiwara TK, Kusumi A.** 2011. Full characterization of GPCR monomer-dimer dynamic equilibrium by single molecule imaging. J. Cell Biol. **192:**463–480. http://dx.doi.org/10.1083/jcb.201009128.
11. **Shi X, Foo YH, Sudhaharan T, Chong SW, Korzh V, Ahmed S, Wohland T.** 2009. Determination of dissociation constants in living zebrafish embryos with single wavelength fluorescence cross-correlation spectroscopy. Biophys. J. **97:**678–686. http://dx.doi.org/10.1016/j.bpj.2009.05.006.
12. **Sudhaharan T, Liu P, Foo YH, Bu W, Lim KB, Wohland T, Ahmed S.** 2009. Determination of in vivo dissociation constant, KD, of Cdc42-effector complexes in live mammalian cells using single wavelength fluorescence cross-correlation spectroscopy. J. Biol. Chem. **284:**13602–13609. http://dx.doi.org/10.1074/jbc.M900894200.
13. **Minton AP.** 2001. The influence of macromolecular crowding and macromolecular confinement on biochemical reactions in physiological media. J. Biol. Chem. **276:**10577–10580. http://dx.doi.org/10.1074/jbc.R100005200.
14. **Minton AP.** 1983. The effect of volume occupancy upon the thermodynamic activity of proteins: some biochemical consequences. Mol. Cell. Biochem. **55:**119–140. http://dx.doi.org/10.1007/BF00673707.
15. **Zimmerman SB, Minton AP.** 1993. Macromolecular crowding: biochemical, biophysical, and physiological consequences. Annu. Rev. Biophys. Biomol. Struct. **22:**27–65. http://dx.doi.org/10.1146/annurev.bb.22.060193.000331.
16. **Bacia K, Kim SA, Schwille P.** 2006. Fluorescence cross-correlation spectroscopy in living cells. Nat. Methods **3:**83–89. http://dx.doi.org/10.1038/nmeth822.
17. **Akagi T, Sasai K, Hanafusa H.** 2003. Refractory nature of normal human diploid fibroblasts with respect to oncogene-mediated transformation. Proc. Natl. Acad. Sci. U. S. A. **100:**13567–13572. http://dx.doi.org/10.1073/pnas.1834876100.
18. **Niwa H, Yamamura K, Miyazaki J.** 1991. Efficient selection for high-expression transfectants with a novel eukaryotic vector. Gene **108:**193–199. http://dx.doi.org/10.1016/0378-1119(91)90434-D.
19. **Johannessen CM, Boehm JS, Kim SY, Thomas SR, Wardwell L, Johnson LA, Emery CM, Stransky N, Cogdill AP, Barretina J, Caponigro G, Hieronymus H, Murray RR, Salehi-Ashtiani K, Hill DE, Vidal M, Zhao JJ, Yang X, Alkan O, Kim S, Harris JL, Wilson CJ, Myer VE, Finan PM, Root DE, Roberts TM, Golub T, Flaherty KT, Dummer R, Weber BL, Sellers WR, Schlegel R, Wargo JA, Hahn WC, Garraway LA.** 2010. COT drives resistance to RAF inhibition through MAP kinase pathway reactivation. Nature **468:**968–972. http://dx.doi.org/10.1038/nature09627.
20. **Gotoh N, Toyoda M, Shibuya M.** 1997. Tyrosine phosphorylation sites at amino acids 239 and 240 of Shc are involved in epidermal growth factor-induced mitogenic signaling that is distinct from Ras/mitogen-activated protein kinase activation. Mol. Cell. Biol. **17:**1824–1831.
21. **Matuoka K, Shibata M, Yamakawa A, Takenawa T.** 1992. Cloning of ASH, a ubiquitous protein composed of one Src homology region (SH) 2 and two SH3 domains, from human and rat cDNA libraries. Proc. Natl. Acad. Sci. U. S. A. **89:**9015–9019. http://dx.doi.org/10.1073/pnas.89.19.9015.
22. **Kamioka Y, Yasuda S, Fujita Y, Aoki K, Matsuda M.** 2010. Multiple decisive phosphorylation sites for the negative feedback regulation of SOS1 via ERK. J. Biol. Chem. **285:**33540–33548. http://dx.doi.org/10.1074/jbc.M110.135517.
23. **Aoki K, Nakamura T, Inoue T, Meyer T, Matsuda M.** 2007. An essential role for the SHIP2-dependent negative feedback loop in neuritogenesis of nerve growth factor-stimulated PC12 cells. J. Cell Biol. **177:**817–827. http://dx.doi.org/10.1083/jcb.200609017.
24. **Terai K, Matsuda M.** 2005. Ras binding opens c-Raf to expose the docking site for mitogen-activated protein kinase kinase. EMBO Rep. **6:**251–255. http://dx.doi.org/10.1038/sj.embor.7400349.
25. **Terai K, Matsuda M.** 2006. The amino-terminal B-Raf-specific region mediates calcium-dependent homo- and hetero-dimerization of Raf. EMBO J. **25:**3556–3564. http://dx.doi.org/10.1038/sj.emboj.7601241.
26. **Torii S, Kusakabe M, Yamamoto T, Maekawa M, Nishida E.** 2004. Sef is a spatial regulator for Ras/MAP kinase signaling. Dev. Cell **7:**33–44. http://dx.doi.org/10.1016/j.devcel.2004.05.019.
27. **Komatsu N, Aoki K, Yamada M, Yukinaga H, Fujita Y, Kamioka Y, Matsuda M.** 2011. Development of an optimized backbone of FRET biosensors for kinases and GTPases. Mol. Biol. Cell **22:**4647–4656. http://dx.doi.org/10.1091/mbc.E11-01-0072.
28. **Yusa K, Rad R, Takeda J, Bradley A.** 2009. Generation of transgene-free induced pluripotent mouse stem cells by the piggyBac transposon. Nat. Methods **6:**363–369. http://dx.doi.org/10.1038/nmeth.1323.

29. **Kinjo M, Sakata H, Mikuni S.** 2011. Basic fluorescence correlation spectroscopy setup and measurement. Cold Spring Harb. Protoc. **2011:**1262–1266. http://dx.doi.org/10.1101/pdb.prot065938.
30. **Bogdanov AM, Bogdanova EA, Chudakov DM, Gorodnicheva TV, Lukyanov S, Lukyanov KA.** 2009. Cell culture medium affects GFP photostability: a solution. Nat. Methods **6:**859–860. http://dx.doi.org/10.1038/nmeth1209-859.
31. **Magde D, Elson EL, Webb WW.** 1974. Fluorescence correlation spectroscopy. II. An experimental realization. Biopolymers **13:**29–61.
32. **Kogure T, Karasawa S, Araki T, Saito K, Kinjo M, Miyawaki A.** 2006. A fluorescent variant of a protein from the stony coral Montipora facilitates dual-color single-laser fluorescence cross-correlation spectroscopy. Nat. Biotechnol. **24:**577–581. http://dx.doi.org/10.1038/nbt1207.
33. **Funahashi A, Morohashi M, Kitano H, Tanimura N.** 2003. CellDesigner: a process diagram editor for gene-regulatory and biochemical networks. Biosilico **1:**159–162. http://dx.doi.org/10.1016/S1478-5382(03)02370-9.
34. **Kitano H, Funahashi A, Matsuoka Y, Oda K.** 2005. Using process diagrams for the graphical representation of biological networks. Nat. Biotechnol. **23:**961–966. http://dx.doi.org/10.1038/nbt1111.
35. **Sauro HM, Hucka M, Finney A, Wellock C, Bolouri H, Doyle J, Kitano H.** 2003. Next generation simulation tools: the Systems Biology Workbench and BioSPICE integration. OMICS **7:**355–372. http://dx.doi.org/10.1089/153623103322637670.
36. **Maeder CI, Hink MA, Kinkhabwala A, Mayr R, Bastiaens PI, Knop M.** 2007. Spatial regulation of Fus3 MAP kinase activity through a reaction-diffusion mechanism in yeast pheromone signalling. Nat. Cell Biol. **9:**1319–1326. http://dx.doi.org/10.1038/ncb1652.
37. **Slaughter BD, Schwartz JW, Li R.** 2007. Mapping dynamic protein interactions in MAP kinase signaling using live-cell fluorescence fluctuation spectroscopy and imaging. Proc. Natl. Acad. Sci. U. S. A. **104:**20320–20325. http://dx.doi.org/10.1073/pnas.0710336105.
38. **Foo YH, Naredi-Rainer N, Lamb DC, Ahmed S, Wohland T.** 2012. Factors affecting the quantification of biomolecular interactions by fluorescence cross-correlation spectroscopy. Biophys. J. **102:**1174–1183. http://dx.doi.org/10.1016/j.bpj.2012.01.040.
39. **Los GV, Encell LP, McDougall MG, Hartzell DD, Karassina N, Zimprich C, Wood MG, Learish R, Ohana RF, Urh M, Simpson D, Mendez J, Zimmerman K, Otto P, Vidugiris G, Zhu J, Darzins A, Klaubert DH, Bulleit RF, Wood KV.** 2008. HaloTag: a novel protein labeling technology for cell imaging and protein analysis. ACS Chem. Biol. **3:**373–382. http://dx.doi.org/10.1021/cb800025k.
40. **Rozakis-Adcock M, McGlade J, Mbamalu G, Pelicci G, Daly R, Li W, Batzer A, Thomas S, Brugge J, Pelicci PG, Schlessinger J, Pawson T.** 1992. Association of the Shc and Grb2/Sem5 SH2-containing proteins is implicated in activation of the Ras pathway by tyrosine kinases. Nature **360:**689–692. http://dx.doi.org/10.1038/360689a0.
41. **Skolnik EY, Lee CH, Batzer A, Vicentini LM, Zhou M, Daly R, Myers MJ, Jr, Backer JM, Ullrich A, White MF, Schlessinger J.** 1993. The SH2/SH3 domain-containing protein GRB2 interacts with tyrosine-phosphorylated IRS1 and Shc: implications for insulin control of ras signalling. EMBO J. **12:**1929–1936.
42. **Cherniack AD, Klarlund JK, Conway BR, Czech MP.** 1995. Disassembly of Son-of-sevenless proteins from Grb2 during p21ras desensitization by insulin. J. Biol. Chem. **270:**1485–1488. http://dx.doi.org/10.1074/jbc.270.4.1485.
43. **Corbalan-Garcia S, Degenhardt KR, Bar-Sagi D.** 1996. Insulin-induced dissociation of Sos from Grb2 does not contribute to the down regulation of Ras activation. Oncogene **12:**1063–1068.
44. **Rozakis-Adcock M, van der Geer P, Mbamalu G, Pawson T.** 1995. MAP kinase phosphorylation of mSos1 promotes dissociation of mSos1-Shc and mSos1-EGF receptor complexes. Oncogene **11:**1417–1426.
45. **Chiu VK, Bivona T, Hach A, Sajous JB, Silletti J, Wiener H, Johnson RL, II, Cox AD, Philips MR.** 2002. Ras signalling on the endoplasmic reticulum and the Golgi. Nat. Cell Biol. **4:**343–350. http://dx.doi.org/10.1038/ncb783.
46. **Hancock JF, Paterson H, Marshall CJ.** 1990. A polybasic domain or palmitoylation is required in addition to the CAAX motif to localize p21ras to the plasma membrane. Cell **63:**133–139. http://dx.doi.org/10.1016/0092-8674(90)90294-O.
47. **Fukuda M, Gotoh Y, Nishida E.** 1997. Interaction of MAP kinase with MAP kinase kinase: its possible role in the control of nucleocytoplasmic transport of MAP kinase. EMBO J. **16:**1901–1908. http://dx.doi.org/10.1093/emboj/16.8.1901.
48. **Dimitri CA, Dowdle W, MacKeigan JP, Blenis J, Murphy LO.** 2005. Spatially separate docking sites on ERK2 regulate distinct signaling events in vivo. Curr. Biol. **15:**1319–1324. http://dx.doi.org/10.1016/j.cub.2005.06.037.
49. **Smith L, Parizi-Robinson M, Zhu MS, Zhi G, Fukui R, Kamm KE, Stull JT.** 2002. Properties of long myosin light chain kinase binding to F-actin in vitro and in vivo. J. Biol. Chem. **277:**35597–35604. http://dx.doi.org/10.1074/jbc.M206483200.
50. **Zhao Y, Bjorbaek C, Moller DE.** 1996. Regulation and interaction of pp90(rsk) isoforms with mitogen-activated protein kinases. J. Biol. Chem. **271:**29773–29779. http://dx.doi.org/10.1074/jbc.271.47.29773.
51. **Fujioka A, Terai K, Itoh RE, Aoki K, Nakamura T, Kuroda S, Nishida E, Matsuda M.** 2006. Dynamics of the Ras/ERK MAPK cascade as monitored by fluorescent probes. J. Biol. Chem. **281:**8917–8926. http://dx.doi.org/10.1074/jbc.M509344200.
52. **Matsunaga-Udagawa R, Fujita Y, Yoshiki S, Terai K, Kamioka Y, Kiyokawa E, Yugi K, Aoki K, Matsuda M.** 2010. The scaffold protein Shoc2/SUR-8 accelerates the interaction of Ras and Raf. J. Biol. Chem. **285:**7818–7826. http://dx.doi.org/10.1074/jbc.M109.053975.
53. **Kinoshita E, Kinoshita-Kikuta E, Takiyama K, Koike T.** 2006. Phosphate-binding tag, a new tool to visualize phosphorylated proteins. Mol. Cell. Proteomics **5:**749–757. http://dx.doi.org/10.1074/mcp.T500024-MCP200.
54. **Jones RB, Gordus A, Krall JA, MacBeath G.** 2006. A quantitative protein interaction network for the ErbB receptors using protein microarrays. Nature **439:**168–174. http://dx.doi.org/10.1038/nature04177.
55. **Porfiri E, McCormick F.** 1996. Regulation of epidermal growth factor receptor signaling by phosphorylation of the ras exchange factor hSOS1. J. Biol. Chem. **271:**5871–5877. http://dx.doi.org/10.1074/jbc.271.10.5871.
56. **Ghosh S, Strum JC, Sciorra VA, Daniel L, Bell RM.** 1996. Raf-1 kinase possesses distinct binding domains for phosphatidylserine and phosphatidic acid. Phosphatidic acid regulates the translocation of Raf-1 in 12-O-tetradecanoylphorbol-13-acetate-stimulated Madin-Darby canine kidney cells. J. Biol. Chem. **271:**8472–8480.
57. **Ghosh S, Xie WQ, Quest AF, Mabrouk GM, Strum JC, Bell RM.** 1994. The cysteine-rich region of raf-1 kinase contains zinc, translocates to liposomes, and is adjacent to a segment that binds GTP-ras. J. Biol. Chem. **269:**10000–10007.
58. **Kolch W.** 2005. Coordinating ERK/MAPK signalling through scaffolds and inhibitors. Nat. Rev. Mol. Cell Biol. **6:**827–837. http://dx.doi.org/10.1038/nrm1743.
59. **Shaul YD, Seger R.** 2007. The MEK/ERK cascade: from signaling specificity to diverse functions. Biochim. Biophys. Acta **1773:**1213–1226. http://dx.doi.org/10.1016/j.bbamcr.2006.10.005.
60. **Shaw AS, Filbert EL.** 2009. Scaffold proteins and immune-cell signalling. Nat. Rev. Immunol. **9:**47–56. http://dx.doi.org/10.1038/nri2473.
61. **Chook YM, Gish GD, Kay CM, Pai EF, Pawson T.** 1996. The Grb2-mSos1 complex binds phosphopeptides with higher affinity than Grb2. J. Biol. Chem. **271:**30472–30478. http://dx.doi.org/10.1074/jbc.271.48.30472.
62. **Sastry L, Lin W, Wong WT, Di Fiore PP, Scoppa CA, King CR.** 1995. Quantitative analysis of Grb2-Sos1 interaction: the N-terminal SH3 domain of Grb2 mediates affinity. Oncogene **11:**1107–1112.
63. **Houtman JC, Yamaguchi H, Barda-Saad M, Braiman A, Bowden B, Appella E, Schuck P, Samelson LE.** 2006. Oligomerization of signaling complexes by the multipoint binding of GRB2 to both LAT and SOS1. Nat. Struct. Mol. Biol. **13:**798–805. http://dx.doi.org/10.1038/nsmb1133.
64. **Lemmon MA, Ladbury JE, Mandiyan V, Zhou M, Schlessinger J.** 1994. Independent binding of peptide ligands to the SH2 and SH3 domains of Grb2. J. Biol. Chem. **269:**31653–31658.
65. **Kiel C, Filchtinski D, Spoerner M, Schreiber G, Kalbitzer HR, Herrmann C.** 2009. Improved binding of raf to Ras. GDP is correlated with biological activity. J. Biol. Chem. **284:**31893–31902. http://dx.doi.org/10.1074/jbc.M109.031153.
66. **Block C, Janknecht R, Herrmann C, Nassar N, Wittinghofer A.** 1996. Quantitative structure-activity analysis correlating Ras/Raf interaction in vitro to Raf activation in vivo. Nat. Struct. Biol. **3:**244–251. http://dx.doi.org/10.1038/nsb0396-244.
67. **Fischer A, Hekman M, Kuhlmann J, Rubio I, Wiese S, Rapp UR.** 2007. B- and C-RAF display essential differences in their binding to Ras: the isotype-specific N terminus of B-RAF facilitates Ras binding. J. Biol. Chem. **282:**26503–26516. http://dx.doi.org/10.1074/jbc.M607458200.
68. **Barbero N, Napione L, Visentin S, Alvaro M, Veglio A, Bussolino F,**

Viscardi G. 2011. A transient kinetic study between signaling proteins: the case of the MEK-ERK interaction. Chem. Sci. **2:**1804–1809. http://dx.doi.org/10.1039/c1sc00268f.
69. **Haystead TA, Dent P, Wu J, Haystead CM, Sturgill TW.** 1992. Ordered phosphorylation of p42mapk by MAP kinase kinase. FEBS Lett. **306:**17–22. http://dx.doi.org/10.1016/0014-5793(92)80828-5.
70. **Mansour SJ, Candia JM, Matsuura JE, Manning MC, Ahn NG.** 1996. Interdependent domains controlling the enzymatic activity of mitogen-activated protein kinase kinase 1. Biochemistry **35:**15529–15536. http://dx.doi.org/10.1021/bi961854s.
71. **Burkhard KA, Chen F, Shapiro P.** 2011. Quantitative analysis of ERK2 interactions with substrate proteins: roles for kinase docking domains and activity in determining binding affinity. J. Biol. Chem. **286:**2477–2485. http://dx.doi.org/10.1074/jbc.M110.177899.
72. **Yoshiki S, Matsunaga-Udagawa R, Aoki K, Kamioka Y, Kiyokawa E, Matsuda M.** 2010. Ras and calcium signaling pathways converge at Raf1 via the Shoc2 scaffold protein. Mol. Biol. Cell **21:**1088–1096. http://dx.doi.org/10.1091/mbc.E09-06-0455.
73. **Gureasko J, Galush WJ, Boykevisch S, Sondermann H, Bar-Sagi D, Groves JT, Kuriyan J.** 2008. Membrane-dependent signal integration by the Ras activator Son of sevenless. Nat. Struct. Mol. Biol. **15:**452–461. http://dx.doi.org/10.1038/nsmb.1418.